

Article

Crystallographic and Seismic Anisotropies of calcite at different depths: a study using Quantitative Texture Analysis by neutron diffraction

Michele Zucali ^{1,2} , Daniel Chateigner ³  and Bachir Ouladdiaf ⁴ 

¹ Dipartimento di Scienze della Terra - Università degli Studi di Milano, Italy; michele.zucali@unimi.it

² Department of Earth and Atmospheric Sciences - University of Houston, Texas - USA; mzucali@uh.edu

³ Laboratoire de Cristallographie et Sciences des Matériaux (CRISMAT), Ecole Nationale Supérieure d'Ingénieurs de Caen University of CAEN - France; daniel.chateigner@ensicaen.fr

⁴ Institut Laue-Langevin - 71 avenue des Martyrs CS 20156, 38042 Grenoble Cedex 9 - France; ouladdiaf@ill.eu

* Correspondence: michele.zucali@unimi.it

Version December 21, 2019 submitted to Minerals

Abstract: Eight samples of limestones and marbles were studied by neutron diffraction to collect Quantitative Texture (i.e., Crystallographic Preferred Orientations or CPO) of calcite deforming at different depths in the crust. We studied the different Texture patterns developed in shear zones at different depth and their influence on seismic anisotropies. Samples were collected in the French and Italian Alps, Apennines, and Paleozoic Sardinian basement. They are characterized by isotropic to highly anisotropic (e.g., mylonite shear zone) fabrics. Mylonite limestones occur as shear zone horizons within the Cenozoic Southern Domain in Alpine thrust-and-fold belts (Italy), the Briançonnais domain of the Western Alps (Italy-France border), the Sardinian Paleozoic back-thrusts or in the Austroalpine intermediate units. The analyzed marbles were collected in the Carrara Marble, in the Austroalpine Units in the Central (Mortirolo) and Western Alps (Valpelline). The temperature and depth of development of fabrics vary from < 100°C, to 800°C and depth from <10 km to about 30 km, corresponding from upper to lower crust conditions. Quantitative Texture Analysis shows different types of patterns for calcite: random to strongly textured. Textured types may be further separated in orthorhombic and monoclinic (Types A and B), based on the angle defined with the mesoscopic fabrics. Seismic anisotropies were calculated by homogenizing the single crystal elastic tensor, using the Orientation Distribution Function calculated by the Quantitative Texture Analysis. The resulting P- and S-waves anisotropies show a wide variability due to the textural types, temperature and pressure conditions, and dip of the shear planes.

Keywords: calcite; seismic anisotropy; texture; CPO; thrust; shear zone; neutron diffraction; crust

1. Introduction

The quantification of the seismic response of rocks is a fundamental task in understanding Earth's structure, from the core to the surface [1]. The large-scale seismic experiments, now with high-resolution arrays, is the most used approach to image the Earth and to resolve the distribution of natural resources in-depth, e.g. water, ore minerals, and oil & gas [2,3]. However, the interpretation of seismic images strongly relies on the knowledge of seismic response of the anisotropic aggregates of minerals composing the rocks, which in turn is intimately related to the textures of rocks [4], as well as on their extrinsic shape preferred features [5]. In the last two decades, a great effort has been made to quantify the seismic response

27 of natural aggregates, chiefly by using the 2-Dimensional approach of the EBSD (Electron Back Scattered
28 Diffraction) to reconstruct the Orientation Distribution Function (e.g. [6–8]). Carbonate rocks occur at the
29 Earth's surface and upper crust levels, as sedimentary cover, but can be found within the intermediate and
30 lower crust, as marbles. Within the upper crust, the tectonic deformation often localizes within carbonate
31 rocks, producing thrust-folds systems [9,10]. Though less diffuse within the metamorphic basements,
32 carbonate rocks are known to be equally crucial at depth because they likely represent weak horizons,
33 often separating tectonometamorphic units [11,12]. For these reasons, the knowledge of the texture and
34 seismic response of carbonate rocks is essential to interpret seismic anisotropy at various depth within the
35 crust [13]. Several works have been dedicated to study the behavior of calcite single crystal, limestones,
36 and marbles at different temperature and pressure [14–19]. A general scheme of the expected textures has
37 been developed, combining natural and numerical data (see [20] and references therein), but data are still
38 needed. Moreover, virtually no work has been dedicated to combining the neutron diffraction textural
39 data with the prediction of seismic velocities through the homogenization of the elastic tensor [21,22].

40 With this contribution, we aim at producing new data related to the textures of carbonate rocks.
41 In particular, we aim at relating different pressure, temperature, and shear geometry conditions of
42 deformation with the type of texture developed. We also aim at investigating the control of texture types on
43 the seismic anisotropies. The presented study will hence provide a reference to interpret measured seismic
44 anisotropy in the continental crust [23], where carbonate rocks might be also involved in accommodating
45 shearing along mylonitic horizons.

46 For this aim, we selected carbonate rocks characterized by fabrics developed at different temperature
47 and pressure conditions and different strain geometries, from pure to simple shear, representing some of
48 the large number of possible combinations in naturally deformed rocks. The samples have been collected
49 mainly in the Alpine system and display a various degree of planar fabrics, developed at different depths
50 within the crust. In this contribution, we will produce new texture data to be included in the general
51 scheme of texture development. Moreover, we will calculate the component of the seismic anisotropies due
52 to the texture by homogenizing the stiffness tensor using the Orientation Distribution Function obtained
53 with the Quantitative Texture Analysis. Finally, we will investigate the influence of the orientation of the
54 foliation plane on the seismic anisotropy [24] at different depth in the crust and with different textures.

55 2. Samples description and geological setting

56 Samples were collected in the French and Italian Alps, Apennines, and Paleozoic basement (Figure 1).
57 Different locations (Figure 1) were chosen to sample carbonate rocks from different crustal levels, from
58 upper/intermediate crust limestones to lower crust high-temperature marbles (Table 1).

59 According to Figure 1, upper crust samples were collected in the Southalpine domain, Sardinia and
60 Helvetic-Dauphinoise (e.g., Triassic and Jurassic limestones). All samples preserve at macroscopic scale
61 their primary features; intermediate crust samples were collected in the Briançonnais domain and in
62 the Central Austroalpine domain, where Mesozoic sediments were involved in the Alpine tectonics at
63 relatively upper levels. However, they still preserve their stratigraphic relations with the surrounding rocks,
64 as sedimentary strata or laminations. The last group of samples, collected in the Carrara metamorphic
65 complex, and in the Western-Central Austroalpine domain, are metamorphic marbles. In this last group,
66 no sedimentary features are preserved.

- 67 • The BAS sample is a light gray crystalline limestone, fine-grained, homogeneous, and free of any
68 planar fabrics at the macroscopic scale, both primary or secondary, as fractures or joints. It is Jurassic
69 in age and it belongs to the External thrust-belt French Subalpine system [25,26]; it is part of the
70 so-called Calcaires "tithoniques" [27]. It was sampled close to Grenoble (France), La Bastille, the
71 southernmost part of the Chartreuse massive. According to the tectonic reconstruction and the local

72 geologic map [27,28], the thrust system developed a km-scale anticline, associated with brittle faults
73 and fracture systems. The BAS sample has been collected within this anticline but far from the brittle
74 system. The fold and thrust system occurred at < 3km depth, at temperature <100°C.

- 75 ● The SOD sample was collected in the Southalpine domain. The sample is part of the Triassic cover,
76 which crops along the entire Southalpine domain. The general interpretation infers the thrust and
77 fold system to convergent tectonics active during the formation of the Alpine system (Figures 1 and
78 2). It was collected within the meter-scale mylonitic horizons associated with a meter to tens of
79 meters asymmetric folds [29]. According to these authors, the thrust horizons occurred at relatively
80 upper depth, not exceeding 5-7 km, corresponding to a maximum of 200°C. The studied sample
81 shows an abrupt change in fabric from undeformed to highly strained domains (Figure 2), often
82 associated with grain-size reduction, pressure-solution, and plastic deformation in carbonate grains,
83 testified by mechanical twinning. These meso- and microstructures support temperatures as high as
84 200°C [30,31]. The kinematics of these thrust horizons have been reconstructed based on stratigraphic
85 and structural constraints, being characterized by strong simple shear components also testified by
86 classical shear indicators, as cm- to mm-scale drag folds and porphyroclasts geometries [32].
- 87 ● SA1 sample was collected in the Sardinia basement. It is part of the Ceroidi Limestone (Gonnesa
88 Fm.), pre-Ordovician protholith of the External Zone. This metasedimentary cover has been deeply
89 involved in the Paleozoic-Variscan tectonics [33]. During the Variscan tectonic activity green-schists
90 metamorphic conditions were attained [34], locally associated with high strain shear horizons, from
91 meters to tens of meters thick [35,36]. The SA1 sample was collected in one of these high strain
92 horizons, made by meta-carbonate limestone. The Variscan deformation developed as pervasive
93 folding systems. However, the SA1 sample was collected far from folds and within the domain where
94 the mylonitic foliation is well visible at macroscopic scale (Figure 2). As qualitative estimates for
95 pressure and temperature, the intermediate limit can be put following the metamorphic evolution of
96 the inner part of the belt, as described by Elter et al [37]. Consequently, a limit of 350°C and 4-5 kbar,
97 corresponding to roughly 12-15 km depth can be used to constrain the development of the fabric in
98 this horizon. Moreover, mesoscopically no asymmetric shear sense indicators have been recognized,
99 supporting the microstructural and textural observations [35], which suggested a pure shear strain.
- 100 ● STE sample was collected in the Central Alps, within the intermediate Austroalpine domain [38].
101 Here the Mesozoic sedimentary cover was involved in the Alpine tectonics, occurring as thick-skinned
102 thrusting of cover and its pre-alpine basement [39]. Thrusting localized along high strain horizons
103 within cover and basement [40]. The temperature conditions of this event were estimated at
104 T=300-350°C at depth=15-20km [41,42]. We collected a sample within the mylonite horizons in
105 the Mesozoic cover, namely the Fraele Fm. It is characterized by a strongly developed mylonite
106 fabric, associated with a meter- to tens of meter folds. A strong transposition of the lithostratigraphic
107 features has been recorded along this horizon [43]. A simple shear component has been described
108 for this deformation based on meso- and microstructural analysis [41]. Sample scale features, as
109 mm-sized drag faults (Figure 2), support the simple shear component.
- 110 ● CC sample was collected in the Western Alps, in the sub-Briançonnais domain. It consists of Jurassic
111 limestone strongly deformed during Alpine thrusting of the external part of the chain [44]. According
112 to [45,46] the External Briançonnais units equilibrated at pressure not exceeding 5 kbar, corresponding
113 to depth <15 km, and T=300-350 °C. Moreover, an overall simple shear kinematics is constrained
114 by map- to micro-scale indicators, extensively described in the area [47-49]; however, the studied
115 sample does not show clear microstructures that could be uniquely related to a simple shear geometry
116 (Figure 2).
- 117 ● P1 was collected in the well-known Carrara marbles quarries. They consist of Mesozoic cover of
118 the Autochthon of the Tuscan Units metamorphosed during the Alpine evolution [50,51]. Km- to

119 meter-scale folding systems have been mapped, and several kinematics reconstructions have been
120 proposed [52] suggesting large scale shear, related to the thrusting of the deep units, resulted in
121 meso- and micro-scale simple shear fabrics (e.g. [20,53]). However, large scale strain partitioning also
122 occurred, allowing large volume of marbles to escape the development of planar or linear fabrics [54].
123 In fact, the studied sample is characterized by isotropic equigranular texture of recrystallized calcite
124 (Figure 2), suggesting a static recrystallization process associated with grain-boundary migration
125 both leading to grain-size increase [32]. Within the Alpi Apuane Metamorphic Complex the estimated
126 conditions of metamorphism point to $T=400-500^{\circ}\text{C}$ at 8-10kbar [50,55,56], corresponding to 25-30 km
127 depth.

- 128 • VP3 and MA1 were both collected in the Austroalpine domain of the Alps [44]. The Austroalpine
129 domain is interpreted as fragments of the pre-alpine continental crust involved in the Alpine
130 subduction-collision system. The collected samples are marbles whose metamorphism has produced
131 during high-temperature Permian-Triassic extension [57]. VP3 was collected in the Valpelline
132 Series, Austroalpine of the Western Alps [58,59], while MA1 was collected in the Languard-Campo,
133 Austroalpine domain of the Central Alps [60]. They are characterized by 0.5-1.5 mm (VP3) to <0.5
134 mm (MA1) grain-size and a strong planar fabric, marked by the shape preferred orientation of
135 calcite and local diopside and quartz (Figure 2). They display diffuse mechanical twinning and
136 undulose extinction, both suggesting grain-scale plastic deformation [32]. Shear indicators are not
137 univocal, MA1 often shows asymmetrical bending of calcite tails around porphyroblast suggesting a
138 component of simple shear, but pure shear cannot be ruled out. Similarly, VP3 displays a less tendency
139 to develop asymmetric microstructures, point to a greater contribution of pure shear. Metamorphic
140 conditions have been quantitatively determined for both samples, VP3 developed at $T=700-800^{\circ}\text{C}$ and
141 $P>6\text{kbar}$, corresponding to >18km depth, while MA1 fabric was estimated to form at $T=600-750^{\circ}\text{C}$
142 and $P=6.5-7.5\text{kbar}$, corresponding to 20-24km depth [58,60].

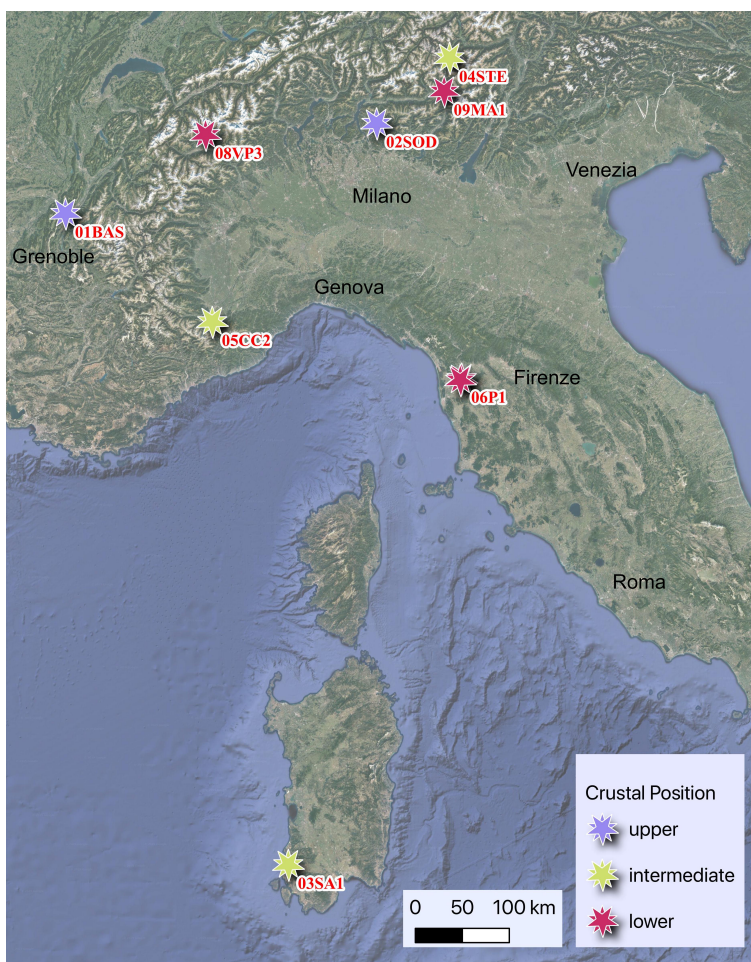


Figure 1. Location and crustal position of the studied samples, see text for explanation

Table 1. List of samples labels with Alpine geological domain, crustal position with depth in km, temperature in °C and shear geometry. Labels are the same as used in figures and text. See text for references on P, T and shear geometry. **Upper crust** for depth <10km at T < 300°C, **intermediate crust** for depth between 10 and 20km and T between 300 and 400 °C, and **lower crust** for depth >20km and T > 400°C

Label	Domain	Crustal Position	Temperature	shear geometry
01BAS	Helvetic-Dauphinoise	upper (<3km)	<100°C	no shear
02SOD	Southalpine	upper (<5-7km)	≈200°C	simple shear
03SA1	Sardinia Basement	intermediate (12-15km)	≈350°C	pure shear
04STE	Austroalpine	intermediate (15-20km)	300-350°C	simple shear
05CC2	Briançonnaise	intermediate (<15km)	300-350°C	pure/simple shear
06P1	Apuane Metamorphic Complex	lower (25-30km)	400-500°C	no shear
08VP3	Austroalpine	lower (>18/20km)	700-800°C	pure/simple shear
09MA1	Austroalpine	lower (20-24km)	600-750°C	simple/pure shear

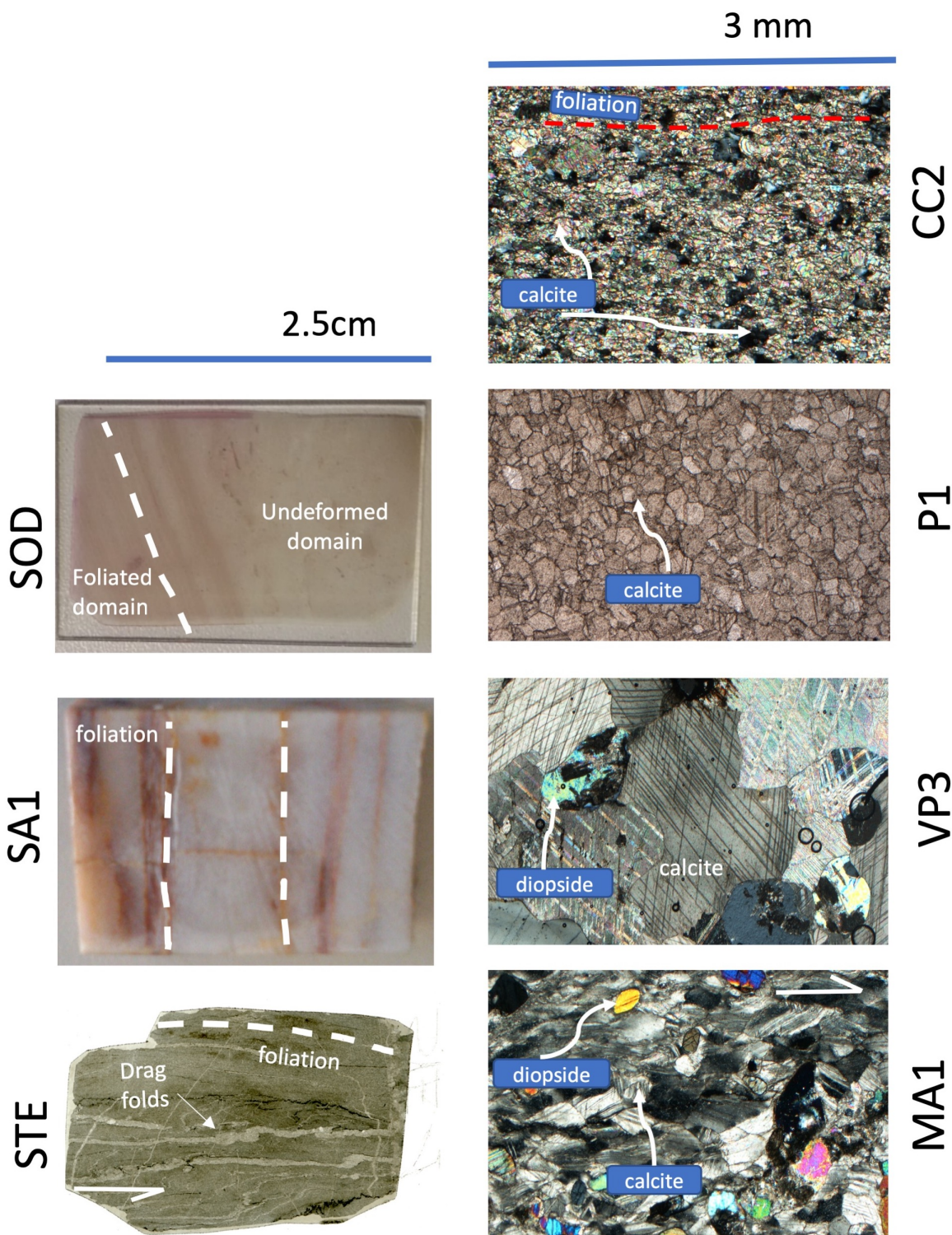


Figure 2. Images of selected samples showing main fabric features as layering or foliation. Scale is indicated. Long side of the image 2.5 cm for STE, SA1 and SOD; long side of the image is 3.0 mm for MA1, VP3, P1 and CC2. MA1, VP3 and CC2 images with crossed polarizers. P1 image with plane polarizers.

143 3. Sample Reference System and Methods

144 The samples were cut in cubes of ≈ 1 cm edge (Figure 3); the three axes of the cube correspond to
 145 the orthonormal reference of the sample. In this orthogonal Sample Reference System, the plane XY
 146 corresponds to the stratification or shear plane, while X direction is taken parallel to the flow direction or
 147 lineation, if it exists (Figure 3). The references in figure 3b are used in all the Pole Figures (Figures 4, 5, 6).
 148 Pole figures display pole densities in multiples of a uniform distribution (mud).

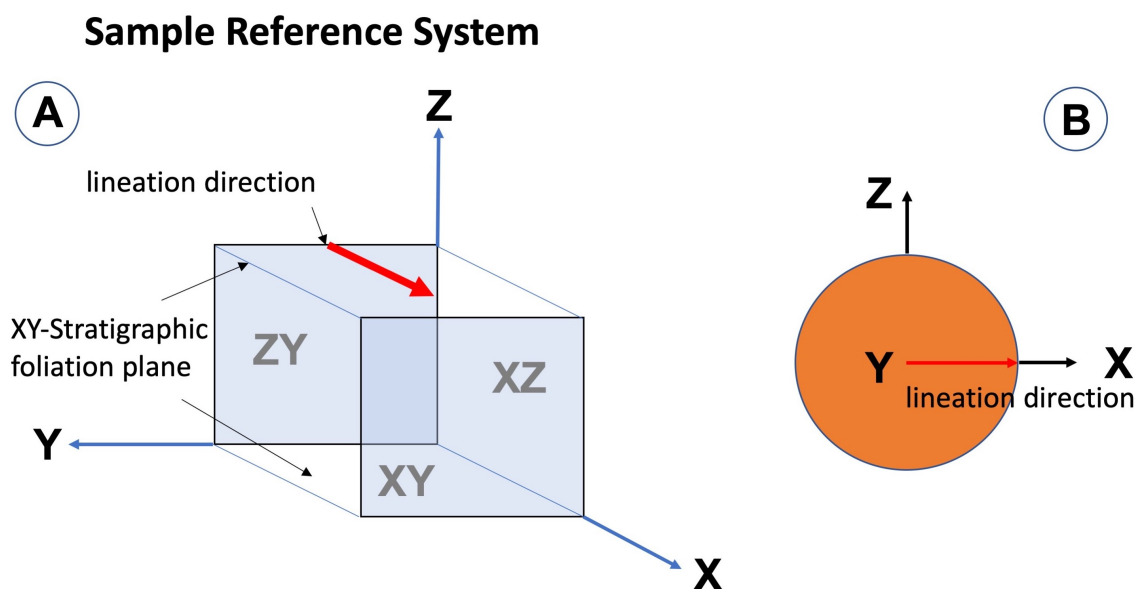


Figure 3. Sample Reference System and Pole figure representation. (a) Sample Reference System showing a simplified cubic sample with respect to the orthogonal reference. X, Y and Z axes are shown (b) Pole figure reference representation with X, Y and Z axes.

149 We used the non-disruptive method of the Quantitative Texture Analysis (QTA) by neutron diffraction.
 150 This method allows the evaluation of the Texture (also called Crystallographic Preferred Orientation,
 151 CPO) of the samples. It has been successfully applied to various types of rocks and synthetic materials:
 152 monomineralic quartzites [61], marbles [20], limestones [62], dunite [63] or glaucophanite [64], in
 153 poly-phasic rocks, as amphibolite [65,66], quartz-feldspatic mylonitic orthogneisses and gabbros [67,68],
 154 subaqueous lavas [69] or sandstones [70]. This procedure uses the high penetration and high flux of
 155 neutrons available at the nuclear reactor at the Institute Laue-Langevin (Grenoble, France) allowing
 156 the measurement of samples with volumes of approximately 1 cm^3 in one to eight hours [71]. Here,
 157 we present the results from the D1B, D19 and D20 diffractometers (<http://www.ill.eu>). The raw data
 158 have been analyzed using the software package MAUD (Materials Analysis Using Diffraction [72]):
 159 diffracted intensities are used to calculate the Orientation Distribution Function (ODF [73]), from which
 160 the representative lattice planes are extracted and represented as Pole Figures (PF). PFs were represented
 161 showing the reference axes from the Sample Reference System (X, Y, Z in Figure 3). The coverage of
 162 the three-dimensional sample space has been acquired differently at the three beam lines (D1B, D19 and
 163 D19), due to their technical specifications. Briefly, D1B works at $\lambda=2.52\text{\AA}$, equipped with a position
 164 sensitive detector, covering a 2θ range of 128° ; D19 is equipped with a very large ($120^\circ \times 30^\circ$) 2-dimensional
 165 position-sensitive detector, and works best in the wavelength range 0.8 to 2.4\AA ; D20 offers wavelength
 166 range 1.4 to 2.1\AA and the position sensitive detector covers 153.6° . The respective angular settings are

167 reported in Table 2. The ODF was calculated using the E-WIMV approach [73]. The reliability of the
 168 refinement is shown by the refinement parameters reported in Table 3. Calcite lattice parameters used for
 169 the refinements are $a=4.9849\text{\AA}$ $c=17.0479\text{\AA}$. 2Theta offset, sample position, and background parameters
 170 were also refined.

Table 2. ILL instrument, setup and DOI. Acquisition time (sec) refers to a single phi-chi position

Sample	Instrument	year	ω°	ϕ°	χ°	acquisition time (sec)	DOI http://doi.ill.fr/10.5291/ILL-DATA
01BAS	D1B	2016	10	0-355	0-90	20	1-02-201 [74]
02SOD	D1B	2016	10	0-355	0-90	20	1-02-201 [74]
03SA1	D19	2014	10	0-355	0-90	10	5-11-397 [75]
04STE	D1B	2016	10	0-355	0-90	20	1-02-163 [76]
05CC2	D1B	2016	10	0-355	0-90	20	1-02-201 [74]
06P1	D1B	2014	10	0-355	0-90	20	1-02-163 [76]
08VP3	D20	2005	10	0-355	0-90	40	no DOI
09MA1	D20	2005	10	0-355	0-90	40	no DOI

Table 3. Quantitative Texture Refinement parameters

Sample	Rb ref	Rexp ref	Rw ewimv	Rb ewimv	F ²
01BAS	7.31	7.56	3.76	4.46	1.04
02SOD	24.6	5.93	2.9	4.0	1.10
03SA1	27.19	25.62	24.11	24.43	1.732
04STE	19.6	6.24	9.53	9.59	1.6
05CC	9.22	3.96	4.11	4.57	1.26
06P1	15.79	6.28	4.85	5.95	1.005
08VP3	31.01	4.05	10.44	11.02	2.17
09MA1	22.83	4.98	12.91	15.73	1.18

171 The Seismic Properties were obtained using petrofabric data, as extensively explained by [7]. Here we
 172 calculated the sample seismic properties by averaging the single crystal elastic tensor [77] weighted by the
 173 ODF, as obtained by Quantitative Texture Analysis by neutron diffraction. In practice, the ODF calculated
 174 using the Maud procedure was used to homogenize the single crystal tensor in Maud. Results for ODF
 175 refinements are reported in Table 3. Although various averaging procedures can be adopted [78], we used
 176 the arithmetic mean of Hill [79]. The resulting homogenized tensors were used in MTEX Matlab Toolbox
 177 [80] to compute and plot seismic properties [81] shown in Figure 6. The same averaged tensors have been
 178 then used to calculate the seismic anisotropies at different dip angles of the foliation plane, simply rotating
 179 the tensors and changing the plane of projection for the pole figure in Figure 8. Pole figures in Figure 8 are
 180 plotted in a way that only the Y axis remains constant and the observer is looking down from the Earth's
 181 surface having the macroscopic foliation plane rotating with respect to the Y axis.

182 As a general consideration, this approach to computing seismic velocities generally produces higher
 183 values when compared to natural samples. The most likely reason for this is that other important factors,
 184 intrinsic and extrinsic, controlling seismic velocities and anisotropies are not included in the calculation.
 185 These factors are fluid pressure, cracks density and their orientation, porosity, grain boundaries geometry
 186 and their shape preferred orientation [5,53,82,83].

187 A thermodynamic approach [66,84] was also used to calculate the seismic properties of a modeled
 188 carbonate rock at different pressure and temperature conditions, roughly corresponding to the estimate
 189 conditions of texture development of the studied samples. We used the PerpleX software package (version

190 6.8.6 [85]) to compute the seismic parameters as dependent on the thermodynamic function G (molar
 191 Gibbs free energy), which is minimized to establish phases, amounts and compositions stable as a function
 192 of pressure and temperature. The software requires a chemical composition of the system as input.
 193 Software and data used for the calculation of phase relations and seismic velocities are freely available
 194 at <http://www.perplex.ethz.ch>. The graphical outputs were obtained using pyWerami source [86]. The
 195 calculated seismic properties correspond to those of a polycrystal rock with no preferred orientations.
 196 An averaged composition of carbonate rocks has been used as the model chemical system [87]. The
 197 model system composition (in wt %) is: $\text{SiO}_2=3.02$, $\text{Al}_2\text{O}_3=0.56$, $\text{FeO}=0.39$, $\text{MgO}=0.75$, $\text{CaO}=52.40$. In the
 198 computation CO_2 is considered saturated and, as solid solutions were chosen Do(HP) dolomite-ankerite
 199 solution, M(HP) for the magnesite-siderite solution, and Cpx(HP) clinopyroxene [88] and [Perplex datafile](#)
 200 [repository](#). Holland and Powell (1998) [88] and successive update [89] (datafile hp62ver.dat at <http://www.perplex.ethz.ch/datafiles/>)
 201 was used as thermodynamic database. A typical output (Figure 7A)
 202 consists of pressure and temperature grid (in this calculation, $P=1-15$ kbar and $T=100-1000^\circ\text{C}$) where the
 203 stable phases and assemblages are shown (i.e., pseudosection). Using the application Werami, which is
 204 part of the PerpleX package [85], specific properties were investigated in the P - T space and plotted in
 205 Figure 7B and 7C. Namely, we investigated the variations of modes, density, V_p and V_s of all phases within
 206 the investigated P - T ranges. Input data for PerpleX calculation may be found as supplementary materials.

207 4. Results

208 4.1. Textures

209 Figure 4 reports the calculated PFs for a single crystal-like of calcite, an aggregate of equigranular
 210 randomly-disposed crystals, and an aggregate of equigranular grains, by a statistical Fibre-Bingham
 211 distribution.

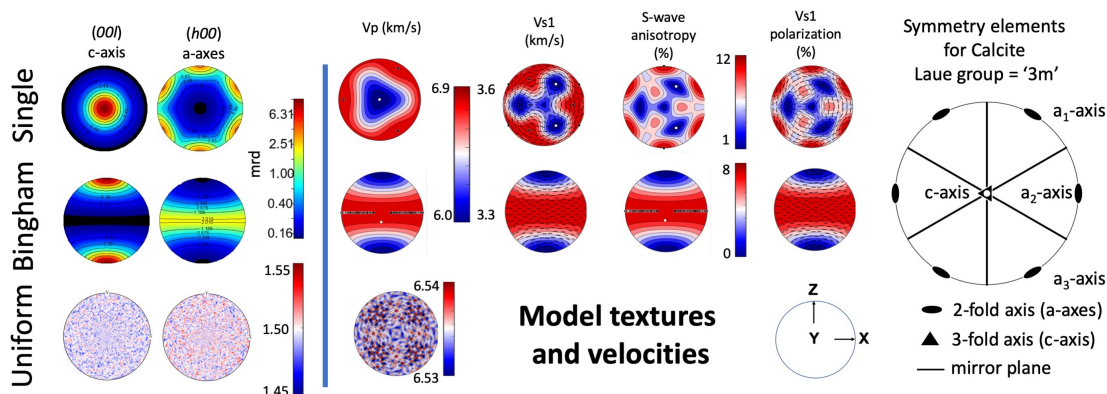


Figure 4. Pole Figures for model Textures and Seismic Velocities for Single Crystal-like, Uniform and Bingham Textured samples. Symmetry elements are shown for calcite crystal

212 They show the contributions to Texture expected by the crystallographic symmetry only or by textures:
 213 i) single crystal distribution is characterized by a strong c-axis maximum and a three-fold axes distribution
 214 in the plane normal to the c-axis; ii) oppositely, a random or uniform distribution of equigranular aggregate
 215 will reduce or obliterate the crystal symmetry anisotropy, producing a random statistical distribution, in
 216 any directions of the 3d space; iii) lastly, an imposed (e.g., tectonic stress) distribution, here represented as

217 the Fibre Bingham distribution [90], will produce strong maxima that follow neither the crystal symmetry
218 and nor a random distribution.

219 Figure 5 reports the pole figures representing the lattice planes (001), (110), (100) texture measured for
220 the studied samples. Calcite texture are commonly expressed showing c- and a-axes distributions (e.g. (001)
221 and (100)) and m-planes (110) since these orientations better describe the deformation mechanisms active
222 during plastic deformation at lattice scale and are commonly reported in the literature. Table 3 reports
223 the R factors and F^2 factor, commonly used in texture analysis to assess the quality of ODF refinement.
224 In general, the samples show different texture distributions and densities but they can be divided into 2
225 principal types: a random distribution (01BAS, 06P1); c-axis textured distribution (02SOD, 03SA1, 04STE,
226 05CC2, 08VP, 09MA). The c-axis textured distribution may be further divided into orthorhombic (02SOD,
227 05CC2, 09MA) and monoclinic symmetry (03SA1, 04STE, 05VP) types. The orthorhombic type (A) is
228 characterized by parallelism between the (001) poles and the Z direction. On the other hand, monoclinic
229 type (B) shows an angle between the (001) poles cluster and the Z direction. Symmetrically, the (100) poles,
230 which generally display a girdle distribution, may lay orthogonal to the Z direction or with an angle,
231 generally 30 to 45 degrees. F^2 values (Table 3) may be used as overall index to assess the randomness of
232 the texture [91,92]. As expected for poorly textured samples, 01BAS, 06P1 have F^2 close to 1 mrd^2 , even
233 though 01BAS displays a minimum amount of preferred orientation. 02SOD, 04STE, 05CC2 and 09MA are
234 characterized by well developed textures, though the F^2 index is relatively low, being between 1.10 and
235 1.26 mrd^2 . Higher F^2 values are shown by 03SA1 and 09MA.

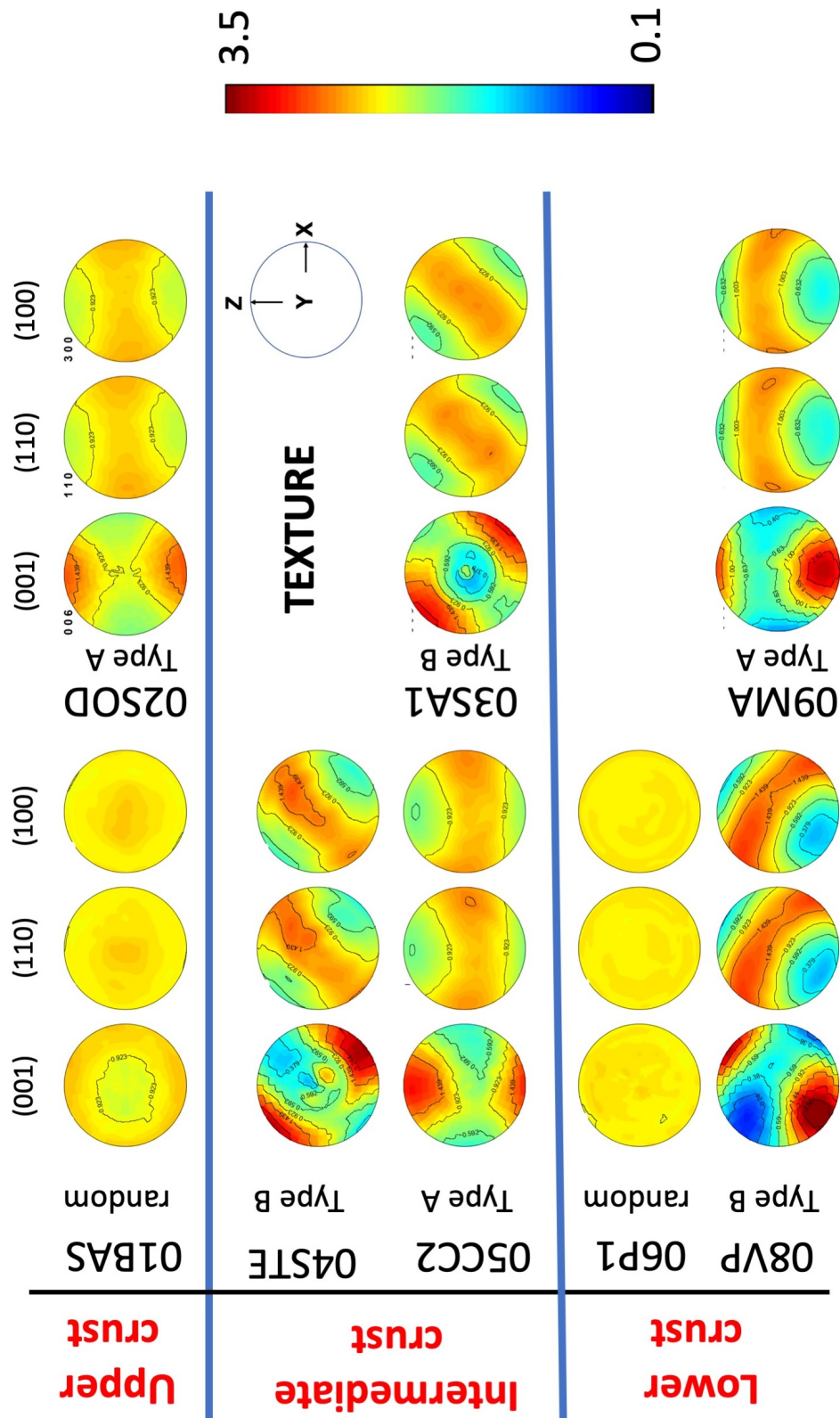


Figure 5. Texture for the studied sample. Pole Figures represents density contours of poles to plane (001), (110), (100), in multiple of uniform distribution (mud). Axes reference as in Figure 3b

236 4.2. Seismic Velocities

237 Figure 6 reports the calculated seismic velocities. Namely, P-wave V_p (km/s), S-wave anisotropy and
238 V_{s1} and V_{s2} polarization. Their distributions closely resemble the main texture feature (Figure 5). In fact,
239 since the c-axis direction is the slowest V_p in the single crystal setting, and the a-axes directions are close
240 to fastest (Figure 3), the general feature that shows up is that the pole to (001) distribution correspond
241 to the slowest directions in the V_p plots. So, the prediction of the slowest direction in carbonate rocks is
242 relatively straightforward since it is influenced by the c-axis distribution. In contrast, S-wave anisotropies
243 are more complex to predict since they result from a combination of textures (Figure 5). Specifically, 02SOD,
244 06P1, 08VP and 09MA display a girdle distribution of the poles to (100) and (110), which correspond to a
245 pronounced direction of fastest propagation. Conversely, 01BAS, 03SA1 and 05CC2 are characterized by
246 single or multiple clusters for S-wave anisotropies, giving a more complex pattern of polarization. 04STE
247 displays a mixed distribution, where a weak fastest S-wave girdle links the two clusters.

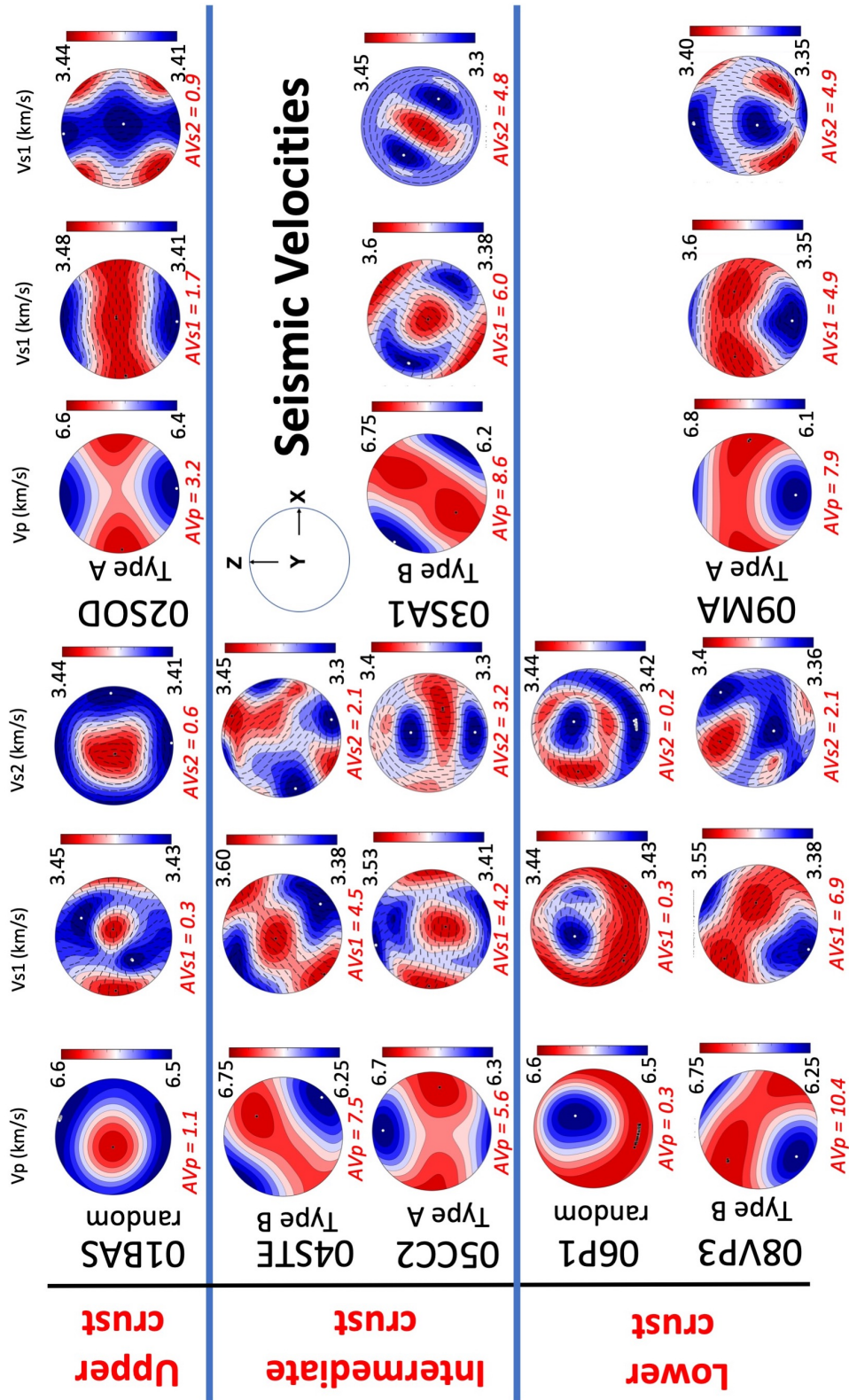


Figure 6. V_p (km/s), V_{s1} (km/s) and V_{s2} (km/s) seismic waves velocities for the studied samples. Anisotropy for V_p (AVp), V_{s1} (AVs1), V_{s2} (AVs2) are calculated as $A = 200 \cdot (\max V - \min V) / (\max V + \min V)$. For AVp $V = V_p$, for AVs1 $V = V_{s1}$, for AVs2 $V = V_{s2}$.

Table 4. Homogenized Elastic Tensors for the studied samples - [GPa] - density = 2.712 g/cm³

Single Crystal					
124.80639	54.72449	51.150898	0	-3.4680943	0
-	124.80639	51.150898	0	3.4680943	0
-	-	100.81746	0	0	0
-	-	-	30.698822	0	3.4680943
-	-	-	-	30.698822	0
-	-	-	-	-	35.04095
Model Bingham					
127.50047	51.043633	55.929905	0	0	0
-	96.653496	51.04301	0	0	0
-	-	127.4964	0	0	0
-	-	-	30.140978	0	0
-	-	-	-	35.78422	0
-	-	-	-	-	30.141603
01BAS					
115.48373	51.741405	52.193005	0.0137869865	-0.15203768	-0.057538427
-	115.00182	52.065735	-0.015753072	-0.070318885	-0.06224491
-	-	117.33802	0.003552162	-0.22920334	0.008067851
-	-	-	32.058846	0.005816382	-0.07812717
-	-	-	-	32.197884	0.013756884
-	-	-	-	-	31.695593
02SOD					
119.29561	51.75047	52.70474	0.09108701	-0.13749328	0.24086875
-	112.01606	51.493103	0.1646471	-0.030619144	0.2721084
-	-	116.93503	0.13448612	-0.15284155	0.118958846
-	-	-	31.385612	0.13175486	-0.03567471
-	-	-	-	32.75555	0.09919309
-	-	-	-	-	31.68194
03SA1					
108.98519	51.129845	53.54879	-0.22707361	0.09098859	4.010708
-	115.68208	54.011932	-0.42028734	0.19944625	4.040168
-	-	120.24887	-0.4792106	0.6209795	1.0868437
-	-	-	34.00615	1.3028204	0.21294828
-	-	-	-	33.391453	-0.24855585
-	-	-	-	-	30.711746
04STE					
114.62599	51.28098	52.65128	0.40403882	-0.24915834	4.076245
-	113.24674	52.87957	1.7690595	0.1510593	2.9629822
-	-	120.20226	1.3745261	-0.33024174	1.3390523
-	-	-	32.772617	1.5227332	0.12351844
-	-	-	-	32.543037	0.45559624
-	-	-	-	-	31.0105
05CC2					

120.331055	52.018433	53.357944	-0.5572579	0.46192774	-0.14939365
-	109.84183	51.32877	-2.052971	0.22327025	-0.38076687
-	-	117.142975	-0.3637613	0.20798893	0.034985803
-	-	-	31.15168	0.02339253	0.23576291
-	-	-	-	33.43074	-0.6357612
-	-	-	-	-	31.877514

06P1

116.18255	52.0272	51.979866	-0.04868714	-0.03236508	-0.011777747
-	116.03572	51.9618	-0.16846395	-0.021853263	-0.021358635
-	51.9618	115.6278	-0.067962535	-0.08895395	-0.020873472
-	-	-	31.94424	-0.021930851	-0.02458574
-	-	-	-	31.965382	-0.053988267
-	-	-	-	-	32.021183

07P2

117.62099	51.808167	52.04327	0.26321256	0.320841	0.538134
-	115.71749	51.596924	0.7797489	0.24568443	0.40074456
-	-	115.65552	0.5507176	0.31947044	0.02256278
-	-	-	31.551678	0.03927036	0.26017663
-	-	-	-	32.037464	0.29400057
-	-	-	-	-	31.800737

08VP3

117.58365	52.024033	53.17902	0.9461038	1.649634	-5.2456484
-	111.576004	52.19252	3.4886246	0.64441526	-4.231288
-	-	119.872314	3.4239075	1.0557145	-1.510464
-	-	-	31.833376	-1.7366006	0.750887
-	-	-	-	32.96562	1.1209756
-	-	-	-	-	31.585485

09MA1

123.13773	51.935154	53.12128	1.066385	0.72052747	-0.34793347
-	108.63644	51.16951	3.118211	0.10843302	-0.30422294
-	-	117.85145	3.0853832	0.26028427	0.001484112
-	-	-	30.831026	-0.014819718	0.1207543
-	-	-	-	33.11233	1.2279662
-	-	-	-	-	31.690102

248 **5. Discussion**249 *5.1. Texture types evolution with temperature, pressure, shear geometry and strain*

250 Texture data reported in Figure 5 fall into the types of calcite texture most commonly described for
251 natural rocks [93] and reported in experimental results [16,17,94,95]. In particular, we separated two types:
252 random, where no or a little preferred orientation is found, and textured, characterized by a strong c-axis
253 maximum and a-axes girdle distribution. Textured types have been further separated in Type A and Type B,
254 to emphasize the relations between Texture and shear plane, as described for pure shear (i.e., orthorhombic
255 geometry, Type A) and simple shear (i.e. monoclinic geometry, Type B) [20,93,96]. Type A and B have been
256 used to infer the deformation regime and the sense of shear (e.g. [97–100]). However, Pieri et al. (2001)

257 [101] demonstrated the risk of simplifying those textural relations with deformational regimes. In fact, the
258 most common calcite deformation mechanisms may allow, even at low temperature, a quick transition
259 from monoclinic to orthorhombic symmetries, even under a simple shear regime and at low strain (>2).
260 Similar observations have been made on naturally deformed marbles [102]. Accordingly, the studied
261 samples also show that discriminating between high temperature (HT) and low temperature (LT) textures
262 is not an easy task. For example, 02SOD, 05CC2 and 09MA1 samples, though their textures developed
263 respectively at $\approx 200^\circ\text{C}$, $300\text{--}350^\circ\text{C}$, and $600\text{--}750^\circ\text{C}$ (Table 1), they all display a similar orthorhombic
264 symmetry; specularly, 04STE, 03SA1, 08VP share the same texture but developed at different temperatures,
265 $300\text{--}350^\circ\text{C}$, $\approx 350^\circ\text{C}$, and $700\text{--}800^\circ\text{C}$ (Table 1). Literature data, between **100 and 400°C** at increasing shear
266 strain, suggest a general evolution from Type A texture, generally far from the shear zone core, to Type
267 B textures and, more often, the coexistence of Type A and B [82]. Type A seems to become dominant at
268 very high shear strain values and very high pressures [16,103]. At low temperature ($<300^\circ\text{C}$) and low
269 pressure ($<3\text{ kbar}$), as in carbonate fault gouges or thrust systems, Type B is generally favorite [104–106]
270 while A and B types start to compete where temperature, pressure and shear strain all overcome certain
271 thresholds. These threshold values are hard to quantify; most likely pressure should exceed 3–4 kbar
272 and shear strain 1–2 [13,16,82,96,103,106]. Similar competing textures were also described for dolomite
273 deforming between $240\text{--}300^\circ\text{C}$ under simple shear geometry [107]. Besides, the recent experimental work
274 of Schuster et al. (2019) [16] shows that very high shear strains (>80) tend to stabilize Type A texture that
275 replaces early A or B types. This experimental work also strongly supports the findings by Ebert et al
276 (2007) [103] that constrained similar evolution from field observations. In particular, Ebert et al (2007) [103]
277 showed evolving random to Type A and B textures as temperature and shear strain increase. Ebert et al
278 (2007) [103] also showed textures similar to those of 04STE and 03SA1 samples where the angle between
279 the c-axis maximum and the Z axis is much higher than typically described.

280 Similar considerations may be done on metamorphic marbles produced at intermediate temperature
281 ($\approx 400\text{--}600^\circ\text{C}$) and pressures related to subduction-collisional tectonics ($\approx 10\text{--}20\text{ kbar}$). In particular, the
282 large literature available on the Carrara Marble allow us to constrain textural types with shear strain
283 geometry and grain size. Large (1–2 mm) to intermediate (0.1–0.5 mm) grain size marbles, characterized
284 by granoblastic textures may show random texture [53,108] as well as Type A [52]. The first most likely
285 due to static annealing or larger scale strain-partitioning and the second associated with grain boundaries
286 migration and subgrain rotation dynamic recrystallization processes [32]. In marbles showing shape
287 preferred orientations and microscopic foliation, the Type A is better developed [20] suggesting a high
288 shear strain condition. Experimental work on Carrara marbles under torsion [109], ranging between 500
289 and 700°C and shear strain from 0 up to 50, support the observations [110] that Type A easily stabilizes
290 at high strain conditions replacing Type B, no matter if coaxial and non-coaxial. Again, this process
291 seems to be more likely occurring at high temperatures ($>500^\circ\text{C}$) [110]. Barnhoorn et al. (2004) [109]
292 also showed that at low temperature ($\approx 500^\circ\text{C}$) random texture may replace Type B textures increasing
293 shear strain. Other intermediate temperature marbles ($400\text{--}500^\circ\text{C}$), from elsewhere (e.g. [11,102,111,112])
294 support this shift from B to A types texture. However, no shear strain constraints are available to include
295 these observations in the above scheme. Higher temperature ($>600^\circ\text{C}$) marbles, similar to samples 08VP3
296 and 09MA1, naturally [22] or experimentally [14,109] deformed do not show a strong shift from B to A
297 type texture. These observations may be taken to support the idea that shear strain most likely controls the
298 textural type, more than temperature. However, more observations are needed to build a valid general
299 scheme. More observations are also needed to produce a solid scheme to relate deformation mechanisms
300 with the observed textures. The texture observed in these samples do not uniquely relate to specific
301 deformation mechanisms. Type A and B textures are present in samples where intra-crystalline slip
302 mechanisms are relevant, as 08VP3 and 09MA1. On the other hand, where twinning is present, together
303 with grain size reduction deformation mechanism (02SOD, 04STE, 05CC2), both Type A and Type B may

304 develop [100]. Moreover, the combination of sub-grain rotation mechanisms, known to be important at
305 similar conditions [16], and grain-boundary migration may have contributed to the observed random
306 texture in P1.

307 5.2. Seismic anisotropy

308 Seismic velocities and anisotropy of carbonate rocks in the studied samples change with texture types
309 (Figure 6). Vp velocities vary from a minimum of 6.1 km/s to a maximum of 6.8 km/s; AVp anisotropy
310 varies between 0.3 and 10.4 (Figure 6). Vs varies from 3.3 and 3.6 km/s, while Vs1 anisotropy varies
311 between 0.3 and 6.8. The direction of maximum Vp varies from parallel to X direction of the fabrics
312 (05CC2, 02SOD, 09MA), corresponding to Type A texture, to more than 45 degrees in the XZ plane (04STE,
313 03SA1, 06P1, 08VP3), for Type B texture. Vp displays a general girdle distribution that roughly describes a
314 plane of max Vp. Max Vp plane changes its orientation even within the same group of Vp max direction.
315 Vp max in Type B samples has an angle with X direction that varies between 20 to 50 degrees. More
316 interestingly, the Vp maximum frequently dips about 20-30 degrees away from the circumference (XZ
317 plane). Similarly, the Vp max girdle plane dips between 20 to 50 degrees from the plane of shear. Besides,
318 Vs velocities frequently show a double to triple maxima distributions. A large literature is available
319 for sedimentary rocks, though the large majority is dedicated to shales and sandstones (see complete
320 review [7]). Similar Vp and Vs values have been measured and calculated for calcite [13,22,82,113,114]
321 at different temperature and depth conditions. Vp velocities most frequently show a girdle distribution
322 of maxima variably dipping to the plane of shear, recalling Type A and Type B distributions. In general,
323 the Vp and Vs velocities overlap with those calculated for our samples, a part for those samples from
324 very shallow depth (<1000m) [113,114] where only after reducing porosity and increasing cementation the
325 Vp values go from low (<5km/s) to higher values, more similar to those here measured and calculated
326 (>6 km/s). These observations support the general idea that carbonate rocks anisotropy also contributes
327 to the overall anisotropy of the crust [7,22,82], at any depths. To further investigate the nature of this
328 anisotropies we calculate the seismic isotropic component by the thermodynamic modeling described in
329 chapter 3. The thermodynamic modeled seismic velocities, Vp and Vs (Figure 7), describe a range of Vp
330 wave velocities from ≈ 6.0 km/s to 6.5 km/s. Vs velocities vary from 2.6 to 3.0 km/s. The P-T plots in
331 Figures 7B and 7C are characterized by three main parts where Vp and Vs vary progressively as a function
332 of the changing mineral assemblages and mode proportion, as described in the pseudosection of Figure
333 7A. The three sectors are characterized by: i) the presence of aragonite instead of calcite a high pressure
334 and low temperature; ii) the association of calcite and dolomite at intermediate temperature and pressure
335 from low to high; ii) the stabilization of clinopyroxene at high temperature, for low to high pressures. In
336 general, Vp and Vs wave velocities decrease moving toward higher temperatures and increase moving
337 toward higher pressures. According to the pressure and temperature constraints for the studied samples
338 (Table 1) we are below the aragonite phase transition and the Vp should vary from 6.0 to 6.5 km/s, and Vs
339 from 2.8 to 3.0 km/s. The calculated values from texture analysis [68,84] as well as those reported in the
340 literature, differ by about 10% from these calculated values. These values are generally closer to measured
341 seismic velocities taken orthogonal to the maximum shear direction (i.e., lineation) [53] or in the more
342 isotropic samples or very shallow sample, dominated by low porosity (<10%) [114]. Consequently, these
343 Vp and Vs can be used as a reference for the isotropic component of carbonate rocks, to investigate the
344 amount of anisotropy to be expected when observing real seismic data for similar rock composition. In
345 general, the analyzed samples show an increase of seismic velocities due only to textural anisotropies
346 that can be about 0.2 to 0.8 km/s for Vp and 0.3 to 0.6 Vs. These results show that seismic properties
347 (e.g., velocities and anisotropies) even for a single rock type (e.g., carbonate rocks) may strongly change in
348 the crust, as function of temperature, pressure, and shear strain, as a result of texture types that strongly

349 control seismic propagation. Similar considerations have been proposed for other rock compositions. In
 350 these rock types specific mineral phases showed preferred orientations that produced relevant deviations
 351 from the isotropic component of the seismic properties (e.g. [7,13,23,84]). This evidence suggests that at
 352 depth there is important overlapping between different rock types in term of their seismic properties, such
 353 that unambiguous determination of geological information from natural seismic data imply a combined
 354 use of many parameters [115]. In addition, it is clear that also the orientation of the macroscopic fabric,
 355 shear foliation, lineation, or any fabric associated with texture in rock-forming minerals play an important
 356 role in defining seismic anisotropies [24,84].

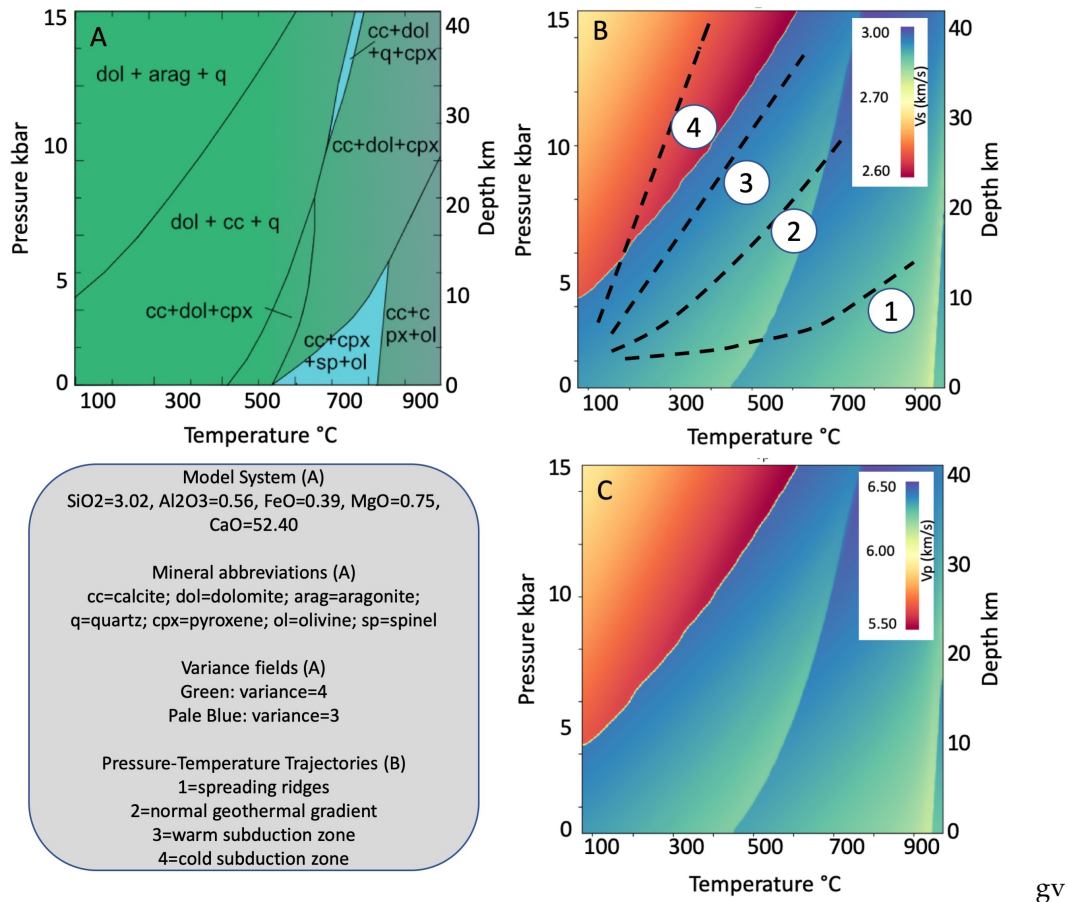


Figure 7. A) Pseudosection calculated using *Perple_X* thermodynamic packages [85]. B) V_s (km/s) seismic waves contour diagram. C) V_p (km/s) seismic waves contour diagram. Geothermal gradients in B after Cloos (1993) [116].

357 To further investigate the relevance of the orientation of the shear plane at different depth in the crust,
 358 we used the approach of Ko and Jung (2015) [24] by rotating the shear flow plane around the Y axis. In
 359 Figure 8 the results are shown by changing the plane of view, from XZ, used in Figures 3, 4, 5, 6, to XY.
 360 Figure 8 shows the progressive variations of the seismic properties by changing the dip angle from 0 to
 361 90 degrees (0, 30, 45, 70, and 90). From the resulting rotated tensors, the components of V_p , V_{s1} and V_{s2}
 362 were read parallel to the horizontal component of the X direction (X' in Figure 8), as well as parallel to the
 363 normal to the Earth's surface (T in Figure 8). Random textures are characterized by a constant V_p and
 364 V_{s2} maxima parallel to the Y direction and the lowest direction being within the $X'T$ plane. The lowest
 365 velocity is always recorded parallel to the vertical T direction, at any dip. A relevant deviation is found

366 for the Vs1 where the highest velocities parallel to T are recorded at dip >45 degrees, while parallel X'
367 at dip <45. Type A shows relatively similar features for samples at different depth, with a general trend
368 with the X' component of Vp which decreases for steep dipping shear zones, while the T component
369 increases, becoming the fastest at depth >30-45 degrees. The Vs1 component generally decreases for the
370 three samples at different depth, but it is steeper for the lower crust sample (e.g., 08MA1). On the other
371 hand, Vs2 components show that the intermediate crust sample 05CC2 has a different trend compared to
372 the other samples. Type B has more diversification than Type A, Vp parallel to T may vary from slowest to
373 fastest, independently by the dip. 08VP3 and 06P1 show the fastest values parallel to T at dip>30. Vs1 and
374 Vs2 fastest are more commonly found at Y for 03SA1 and 04STE intermediate crust samples, while in 06P1
375 Vs1 fastest velocities describe a girdle close to the X'T plane at any dip and in 08VP3 sample become closer
376 to T at dip>45. Vs2 velocities Vs2 fastest velocities are in the direction of Y for 03SA1 at any dip while
377 they are highly variable for the sample 04STE. Girdles with maxima characterize Vs2 in 06P1 and 08VP3,
378 producing highly heterogeneous distribution at different dip.

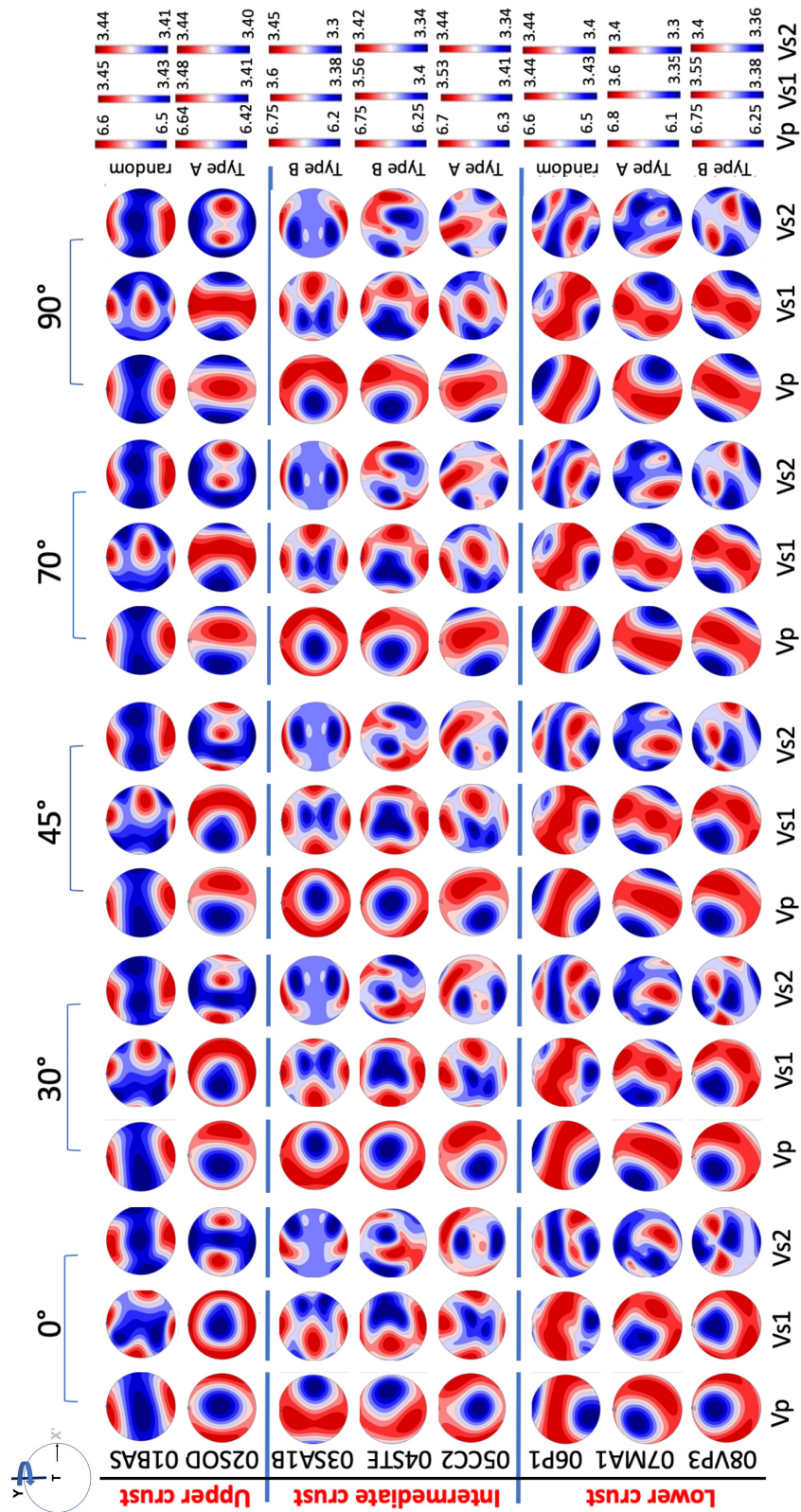


Figure 8. Pole Figures representing the P- and S- (S1 and S2) seismic velocities for calcite at different depth and dipping angle of the main macroscopic fabric plane (e.g. shear plane or stratification). X' correspond to the horizontal component of the X fabric axis while T correspond to the normal to the horizontal surface.

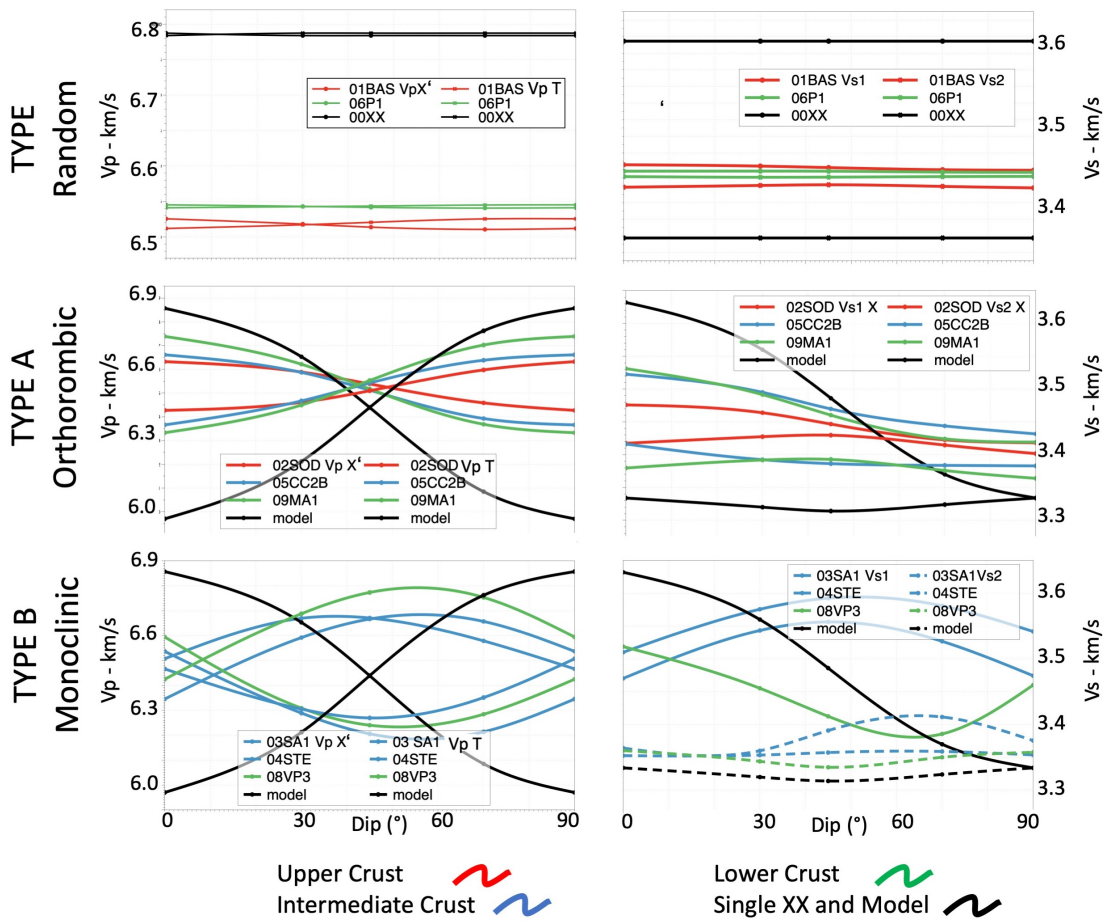


Figure 9. Vp components propagating horizontally (X' component) and vertically (T component) - Vs1 and Vs2 horizontal component (of X)X'. See text for explanation

379 In the Type B distribution, the lower crust sample 09VP3 displays an opposite trend to the intermediate
 380 crust samples 03SA1 and 04STE. In particular, while for the intermediate crust samples the horizontal
 381 Vp and Vs1 values increase from 0 to 45-50 degrees and then decrease approaching vertical dipping,
 382 the lower crustal sample 08VP3 starts decreasing and then, at about 60 degrees dip, increases. These
 383 heterogeneities also occur for vertical Vp and Vs2 components. The Vp vertical component closely mirrors
 384 the Vp horizontal, while the Vs2 components are less sensitive to the dip variation, being in a smaller
 385 interval, generally < 0.1 km/s.

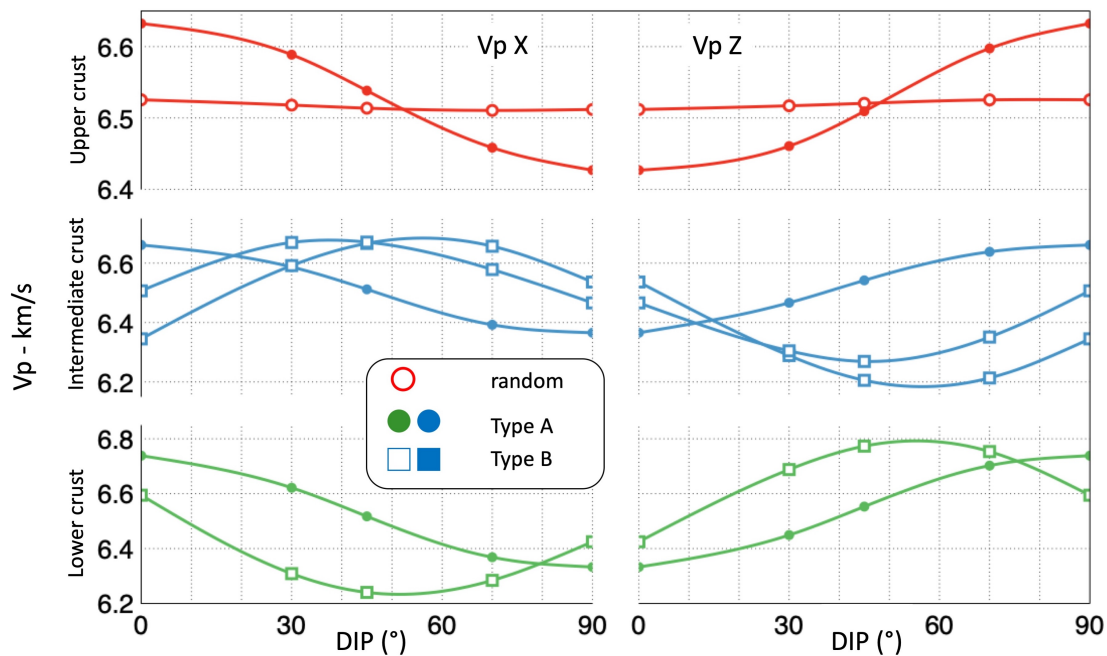


Figure 10. Vp crustal section. upper crust = red, intermediate crust = blue, lower crust = green. Texture types: A = hollow circle; A = full circle; B = hollow square

386 Figure 10 represents the Vp velocities at different depths, at varying dip. From 0 to 15 degrees dipping
 387 of the shear planes, as those generally developed along the flat part of thrust systems [9], the Type A
 388 textures produce higher Vp velocities propagating horizontally, parallel to X' component (Figure 8) and
 389 slower parallel to the normal to the topographic surface (T component in Figure 8). This setting does not
 390 change with depth, while the fastest Vp velocities are recorded at depth (i.e., lower crust). This pattern is
 391 reversed at different dip angles: upper crust at 50 degrees, intermediate crust between 20 and 30 degrees,
 392 and the lower crust at 80 degrees. At intermediate crust conditions, this flip may correspond to the
 393 evolution of the thrust system from flats to ramps. The change of dip correspond to a substantial increase
 394 of Vp velocities parallel to X', from 6.4 to 6.7 km/s. At the same depths, it corresponds a decrease parallel
 395 to T for rocks having a Type B texture pattern. Oppositely, at depth, both Type A and B produce an overall
 396 decrease of horizontally propagating velocities, from 6.8 to 6.3 km/s and from 6.6 to 6.2 km/s, respectively.
 397 Type B reaches its minimum at 50 degrees and then increases slowly approaching vertical dipo. In general,
 398 steep dipping shear zones, as those in transtensional or transpressional systems (e.g., positive and negative
 399 flower structures), will produce slower or at maximum equal Vp velocities propagating horizontally (X')
 400 than shear zone within the same system but with lower dipping angles (Figure 10). Figure 11 represents
 401 the evolution of Vp seismic velocities (vertical component T) with depth at changing dip angles. Figure
 402 11 also reports the predicted P-wave velocities in the continental crust as modeled by Lloyd et al. (2011)
 403 [23] for 'rock recipes'. Vertical red boxes correspond to Vp ranges for middle to lower crust proposed by
 404 Rudnick & Fountain (1995)[117]. Two aspects arise from this image. Firstly, carbonate rock may overlap
 405 with average rock types or 'recipes' at various depth in the continental crust. Large discrepancies to these
 406 overlapping may arise by the dipping of the shear planes. At similar depths, Vp velocities may differ of
 407 about 0.3-0.5 km/s, only due to different dipping. Secondly, a specific patten is reproduced by Type A
 408 texture, at any depth. Type A texture shows is characterized by an increase of Vp velocities as the dipping
 409 angle increases. This pattern is reproduced at the three different depths our samples represent. Moreover,
 410 Types B displays more variability in the way seismic velocities change with dipping of the shear plane.

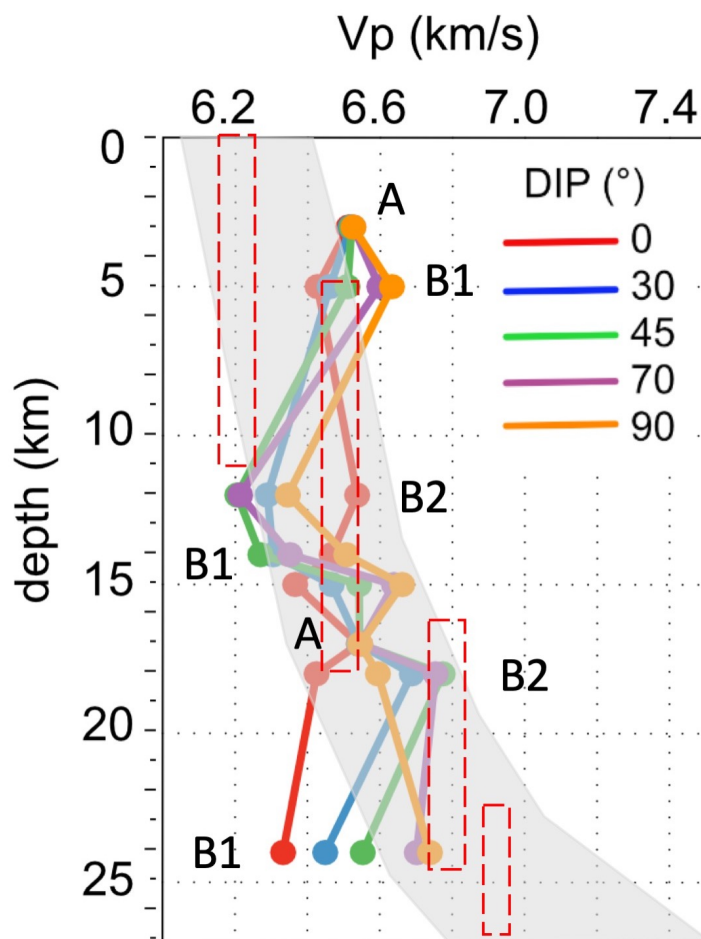


Figure 11. P-wave velocity propagating vertically (T component of Figure 8) crustal profile based on the data presented in this work for carbonate rocks at different depth and dip angle of the shear plane. Grey are correspond to the predicted P-wave velocities in the continental crust as modeled by Lloyd et al. (2011) [23]. Vertical red boxes correspond to Vp ranges for middle to lower crust Rudnick & Fountain (1995)[117]. A, A, and B texture Types described in the text.

411 6. Conclusions

- 412
- 413
- 414
- 415
- 416
- 417
- 418
- 419
- 420
- 421
- 422
- 423
- 424
- Eight samples of limestones and marbles were studied by neutron diffraction. We collected Texture of naturally deformed calcite at different depths in the crust, from upper to lower crust.
 - Different Texture patterns were recognized, from random to strongly textured (Type B); the latter, with orthorhombic (Type A) or monoclinic (Type B) symmetries. Seismic anisotropies were calculated using the Orientation Distribution Function to homogenize the elastic tensor of calcite.
 - A wide variability of seismic anisotropies arise from the various textural types, crustal positions and dipping of the shear planes.
 - These results may be valuably used to guess geometry of shear zones at upper to depth for carbonate rocks or at deeper crustal levels where thick carbonatic horizons are involved localizing deformation (Figure 11).
 - This work suggests that at depth, even for carbonate rocks, there is an important overlapping between different rock types in term of their seismic properties (Figure 11); unambiguous determination of geological information from natural seismic must consider the orientation of the macroscopic fabric,

425 shear foliation, lineation, or any fabric associated with texture playing a role in developing seismic
 426 anisotropies [24,84].

- 427 • More work still needs to be done to include other parameters influencing seismic anisotropies,
 428 intrinsic and extrinsic, to build a database of natural rocks properties [5–7,13,23].
- 429 • Lastly, texture types may produce unique seismic velocities pattern. For example, Type A (Figure 11)
 430 produce a unique pattern at any depth, characterized by an increase of Vp velocities (e.g., 6.3 to 6.8
 431 at 20-25km depth) as the dipping angle increases. Future studies may show if these singular pattern
 432 might be used to better constrain the interpretation of seismic profiles.

433 **Author Contributions:** All authors participated in the preparation of this manuscript. M.Z. conducted sample
 434 collection, collaborated neutron experiments, data analysis and prepared the first version of the manuscript. D.C.
 435 worked on neutron experiments and data analysis. B.O. worked on neutron experiments and data analysis

436 **Funding:** Neutron experiments were funded by ILL (www.ill.eu)

437 **Acknowledgments:** Two anonymous reviewers are greatly thanked for their help to produce the present form

438 **Conflicts of Interest:** The authors declare no conflict of interest.

439 References

- 440 1. Lowrie, W. *Fundamentals of Geophysics*; 2007. doi:10.1017/cbo9780511807107.
- 441 2. Sun, L.; Fang, C.; Sa, L.; Yang, P.; Sun, Z. Innovation and prospect of geophysical technology in the
 442 exploration of deep oil and gas. *Shiyou Kantan Yu Kaifa/Petroleum Exploration and Development* **2015**, *42*, 414–424.
 443 doi:10.1016/S1876-3804(15)30038-0.
- 444 3. Kendair, J.M.; Maddock, J.; Hall, S.A.; Fisher, Q.J. Seismic anisotropy as an indicator of reservoir quality in
 445 siliciclastic rocks. *69th European Association of Geoscientists and Engineers Conference and Exhibition 2007: Securing
 446 The Future. Incorporating SPE EUROPEC 2007* **2007**, *5*, 2614–2618. doi:10.1144/SP292.7.
- 447 4. Okaya, D.; Vel, S.S.; Song, W.J.; Johnson, S.E. Modification of crustal seismic anisotropy by geological structures
 448 ("structural geometric anisotropy"). *Geosphere* **2019**, *15*, 146–170. doi:10.1130/GES01655.1.
- 449 5. Faccenda, M.; Ferreira, A.M.; Tisato, N.; Lithgow-Bertelloni, C.; Stixrude, L.; Pennacchioni, G. Extrinsic Elastic
 450 Anisotropy in a Compositionally Heterogeneous Earth's Mantle. *Journal of Geophysical Research: Solid Earth*
 451 **2019**, *124*, 1671–1687. doi:10.1029/2018JB016482.
- 452 6. Brownlee, S.J.; Schulte-Pelkum, V.; Raju, A.; Mahan, K.; Condit, C.; Orlandini, O.F. Characteristics of deep
 453 crustal seismic anisotropy from a compilation of rock elasticity tensors and their expression in receiver functions.
 454 *Tectonics* **2017**, *36*, 1835–1857. doi:10.1002/2017TC004625.
- 455 7. Almqvist, B.S.; Mainprice, D. Seismic properties and anisotropy of the continental crust: Predictions based on
 456 mineral texture and rock microstructure. *Reviews of Geophysics* **2017**, *55*, 367–433. doi:10.1002/2016RG000552.
- 457 8. Prior, D.J.; Mariani, E.; Wheeler, J. EBSD in the Earth Sciences: Applications, Common Practice,
 458 and Challenges EBSD in the Earth Sciences: Applications, Common Practice, and Challenges **2010**.
 459 doi:10.1007/978-0-387-88136-2.
- 460 9. Suppe, J. Geometry and Kinematics of fault-bend folding. *American Journal of Science* **1983**, *283*, 681–721.
- 461 10. Smith, S.A.; Di Toro, G.; Kim, S.; Ree, J.H.; Nielsen, S.; Billi, A.; Spiess, R. Coseismic recrystallization during
 462 shallow earthquake slip. *Geology* **2013**, *41*, 63–66. doi:10.1130/G33588.1.
- 463 11. Busch, J.P.; van der Pluijm, B.a. Calcite textures, microstructures and rheological properties of marble mylonites
 464 in the Bancroft shear zone, Ontario, Canada. *Journal of Structural Geology* **1995**, *17*, 677–688.
- 465 12. Bestmann, M.; Kunze, K.; Matthews, A. Evolution of a calcite marble shear zone complex on Thassos Island,
 466 Greece: Microstructural and textural fabrics and their kinematic significance. *Journal of Structural Geology* **2000**,
 467 *22*, 1789–1807. doi:10.1016/S0191-8141(00)00112-7.
- 468 13. Almqvist, B.S.; Hirt, A.M.; Herwegh, M.; Ebert, A.; Walter, J.M.; Leiss, B.; Burlini, L. Seismic anisotropy in the
 469 Morcles nappe shear zone: Implications for seismic imaging of crustal scale shear zones. *Tectonophysics* **2013**,
 470 *603*, 162–178. doi:10.1016/j.tecto.2013.05.025.

- 471 14. Barber, D.J.; Wenk, H.R.; Gomez-Barreiro, J.; Rybacki, E.; Dresen, G. Basal slip and texture development
472 in calcite: New results from torsion experiments. *Physics and Chemistry of Minerals* **2007**, *34*, 73–84.
473 doi:10.1007/s00269-006-0129-3.
- 474 15. Pieri, M.; Kunze, K.; Burlini, L.; Stretton, I.; Olgaard, D.L.; Burg, J.P.; Wenk, H.R. Texture development of calcite
475 by deformation and dynamic recrystallization at 1000 K during torsion experiments of marble to large strains.
476 *Tectonophysics* **2001**, *330*, 119–140.
- 477 16. Schuster, R.; Habler, G.; Schafler, E.; Abart, R. Microstructural and textural evolution of calcite deformed to high
478 shear strain by high-pressure torsion. *Journal of Structural Geology* **2019**, *118*, 32–47. doi:10.1016/j.jsg.2018.09.003.
- 479 17. Schmid, S.M.; Panozzo, R.; Bauer, S. Simple shear experiments on calcite rocks: rheology and microfabrics. *J.*
480 *Struct. Geol.* **1987**, *9*, 747–778.
- 481 18. Ferrero, A.M.; Migliazza, M.; Spagnoli, A.; Zucali, M. Micromechanics of intergranular cracking due
482 to anisotropic thermal expansion in calcite marbles. *Engineering Fracture Mechanics* **2014**, *130*, 42–52.
483 doi:10.1016/j.engfracmech.2014.01.004.
- 484 19. Lutterotti, L.; Matthies, S.; Wenk, H.R.; Schultz, a.S.J.; Richardson, J.J.W. Combined texture and structure
485 analysis of deformed limestone from time-of-flight neutron diffraction spectra. *Journal of Applied Physics* **1997**,
486 *81*, 594–600.
- 487 20. Leiss, B.; Molli, G. 'High-temperature' texture in naturally deformed Carrara marble from the Alpi Apuane,
488 Italy. *Journal of Structural Geology* **2002**, *25*, 649–658.
- 489 21. Matthies, S.; Humbert, M. On the Principle of a Geometric Mean of Even-Rank Symmetric Tensors for Textured
490 Polycrystals. *Journal of Applied Crystallography* **1995**, *28*, 254–266. doi:10.1107/S0021889894009623.
- 491 22. Punturo, R.; Kern, H.; Cirrincione, R.; Mazzoleni, P.; Pezzino, A. P- and S-wave velocities and densities in
492 silicate and calcite rocks from the Peloritani Mountains, Sicily (Italy): The effect of pressure, temperature and
493 the direction of wave propagation. *Tectonophysics* **2005**, *409*, 55–72. doi:10.1016/j.tecto.2005.08.006.
- 494 23. Lloyd, G.E.; Butler, R.W.H.; Casey, M.; Tatham, D.J.; Mainprice, D. Constraints on the seismic properties of the
495 middle and lower continental crust. *From: Prior, D. J., Rutter, E. H. & Tatham, D. J. (eds) Deformation Mechanisms,*
496 *Rheology and Tectonics: Microstructures, Mechanics and Anisotropy. Geological Society, London Special Publications.*
497 **2011**, *360*, 7–32.
- 498 24. Ko, B.; Jung, H. Crystal preferred orientation of an amphibole experimentally deformed by simple shear.
499 *Nature Communications* **2015**, *6*, 1–10. doi:10.1038/ncomms7586.
- 500 25. Debrand-Passard, S.; Courbouleix, S.; Lienhardt, M. Synthèse géologique du Sud-Est de la France: Mémoires
501 BRGM, Orléans **1984**. pp. 1–125.
- 502 26. Courjault, T.; Grosheny, D.; Ferry, S.; Sausse, J. Detailed anatomy of a deep-water carbonate breccia lobe (Upper
503 Jurassic, French subalpine basin). *Sedimentary Geology* **2011**, *238*, 156–171. doi:10.1016/j.sedgeo.2011.04.010.
- 504 27. BRGM. La carte géologique à 1/50000 GRENOBLE est recouverte par la coupure de la carte géologique de la
505 France à 1/80000. *BRGM* **1970**.
- 506 28. Jourdon, A.; Rolland, Y.; Petit, C.; Bellahsen, N. Style of Alpine tectonic deformation in the Castellane
507 fold-and-thrust belt (SW Alps, France): Insights from balanced cross-sections. *Tectonophysics* **2014**, *633*, 143–155.
508 doi:10.1016/j.tecto.2014.06.022.
- 509 29. Gaetani, M.; Sciunnach, D.; Bini, A.; Rossi, S. Foglio 076 Lecco. Note illustrative della Carta Geologica d'Italia
510 alla scala 1: 50.000 - ISPRA **2012**.
- 511 30. Burkhard, M. Calcite twins, their geometry, appearance and significance as stress-strain markers and indicators
512 of tectonic regime: a review. *Journal of Structural Geology* **1993**, *15*, 351–368.
- 513 31. Ferrill, D. A., Morris, A. P., Evans, M. A., Burkhard, M., Groshong Jr, R. H., & Onasch, C.M. Calcite twin
514 morphology: a low-temperature deformation geothermometer. *Journal of Structural Geology* **2004**, *26*, 1521–1529.
- 515 32. Passchier, C.; Trouw, R. *Microtectonics*; Vol. 275, 2005; p. 366. doi:10.1007/978-3-662-08734-3.
- 516 33. Carmignani, L.; Oggiano, G.; Barca, S.; Conti, P.; Eltrudis, A.; Funedda, A.; Pasci, S.; Salvadori, I. Memorie
517 Descrittive Della Carta Geologica D'Italia. *Note illustrative della Carta Geologica della Sardegna a scala 1:200.000*
518 **2001**, p. 283.

- 519 34. Franceschelli, M.; Puxeddu, M.; Cruciani, G. Variscan metamorphism in Sardinia, Italy: Review and discussion.
520 *Journal of the Virtual Explorer* **2005**, pp. 1–35. doi:10.3809/jvirtex.2005.00121.
- 521 35. Lebit, H. On fold and strain interference patterns in the Paleozoic rocks of Iglesias (SW Sardinia). *Tesi di*
522 *Dottorato, ETH Zurich* **1995**.
- 523 36. Carmignani, L.; Conti, P.; Funedda, A.; Oggiano, G.; Pasci, S. La geologia della Sardegna - Geological Field
524 *Tips. Geological Field Trips* **2012**, *4*, 104. doi:10.3301/GFT.2012.04.
- 525 37. Elter, F.M.; Corsi, B.; Cricca, P.; Muzio, G. The south-western alpine foreland: Correlation between two sectors
526 of the variscan chain belonging to “stable Europe”: Sardinia(-)Corsica and the Maures Massif (South-Eastern
527 France). *Geodinamica Acta* **2004**, *17*, 31–40. doi:10.3166/ga.17.31-40.
- 528 38. Polino, R.; Dal Piaz, G.V.; Gosso, G. Tectonic erosion at the Adria margin and accretionary processes for the
529 Cretaceous orogeny of the Alps. In *Deep structure of the Alps*; Roure, F.; Heitzmann, P.; Polino, R., Eds.; Number
530 156, 1990; pp. 345–367.
- 531 39. Schmid, S.M.; Haas, R. Transition from near-surface thrusting to intrabasement decollement, Schlinig Thrust,
532 Eastern Alps. *Tectonics* **1989**, *8*, 697–718.
- 533 40. Conti, P.; Manatschal, G.; Pfister, M. Synrift sedimentation, Jurassic and Alpine tectonics in the central Ortler
534 *Nappe*, (Eastern Alps, Italy). *Eclogae Geologicae Helvetiae* **1994**, *87*, 63–90.
- 535 41. Conti, P. The Austroalpine Ortler Nappe and the tectonic evolution of the Engadine Dolomites (Switzerland -
536 ITALY). PhD thesis, 1997.
- 537 42. Berra, F.; Jadoul, F. Stratigraphy, paleogeography and tectonic setting of the Norian succession of the Ortles
538 *Nappe* (Central Austroalpine, Lombardy, Northern Italy). *Memorie di Scienze Geologiche Padova* **1999**, *51*, 78–89.
- 539 43. Montrasio, A.; Berra, F.; Cariboni, M.; Ceriani, M.; Deichmann, N.; Ferliga, C.; Gregnanin, A.; Guerra, S.;
540 Guglielmin, M.; Jadoul, F.; Longhin, M.; Mair, V.; Mazzoccola, D.; Sciesa, E.; Zappone, A. Note Illustrative dalla
541 *Carta Geologica d'Italia alla scala 1:50.000 Foglio 24 CARG. ISPRA* **2012**, *24*, 150.
- 542 44. Bigi, G.; Castellarin, A.; Coli, M.; Dal Piaz, G.V.; Sartori, R.; Scandone, P.; Vai, G.B. Structural Model of Italy,
543 sheets 1-2, Progetto Finalizzato Geodinamica. *CNR* **1990**.
- 544 45. Piana, F.; Battaglia, S.; Bertok, C.; D'atri, A.; Ellero, A.; Leoni, L.; Martire, L.; Perotti, E. Illite (KI) and chlorite
545 (AI) "crystallinity" indices as a constraint for the evolution of the External Briançonnais Front in Western
546 *Ligurian Alps* (NW Italy). *Italian Journal of Geosciences* **2014**, *133*, 445–454. doi:10.3301/IJG.2014.21.
- 547 46. Michard, A.; Avigad, D.; Goffé, B.; Chopin, C. The high-pressure metamorphic front of the south Western
548 *Alps* (Ubaye-Maira transect, France, Italy). *Schweizerische Mineralogische und Petrographische Mitteilungen* **2004**,
549 *84*, 215–235.
- 550 47. Bertok, C.; Musso, A.; D'atri, A.; Martire, L.; Piana, F. Geology of the Colle di Tenda – monte marguareis area
551 *(Ligurian Alps, NW Italy)*. *Journal of Maps* **2018**, *14*, 542–551. doi:10.1080/17445647.2018.1500497.
- 552 48. Carminati, E.; Gosso, G. Structural map of a Ligurian Briançonnais cover nappe (Conca delle Carsene, Monte
553 *Marguareis, Ligurian Alps, Italy)* and explanatory notes. *Mem. Sc. Geol. Padova* **2000**, *52-1*, 93–99.
- 554 49. Carminati, E. Incremental strain analysis using two generations of syntectonic coaxial fibres: An example
555 *from the Monte Marguareis Briançonnais cover nappe (Ligurian Alps, Italy)*. *Journal of Structural Geology* **2001**,
556 *23*, 1441–1456. doi:10.1016/S0191-8141(01)00010-4.
- 557 50. Molli, G.; Giorgetti, G.; Meccheri, M. Tectono-metamorphic evolution of the Alpi Apuane Metamorphic
558 *Complex: New data and constraints for geodynamic models*. *Bolletino della Società Geologica Italiana* **2001**,
559 *1*, 789–800.
- 560 51. Di Pisa, A.; Franceschelli, M.; Leoni, L.; Meccheri, M. Regional variation of the metamorphic temperatures
561 *across the Tuscanid I Unit and its implications on the alpine metamorphism (Apuan Alps, N-Tuscany)*. *Neues*
562 *Jahrbuch für Mineralogie, Ab-handlungen* **1985**, *151*, 197–211.
- 563 52. Molli, G.; Conti, P.; Giorgetti, G.; Meccheri, M.; Oesterling, N. Microfabric study on the deformational and
564 *thermal history of the Alpi Apuane marbles (Carrara marbles), Italy*. *Journal of Structural Geology* **2000**,
565 *22*, 1809–1825.
- 566 53. Burlini, L.; Kunze, K. Fabric and seismic properties of Carrara marble mylonite. *Physics and Chemistry of the*
567 *Earth, Part A: Solid Earth and Geodesy* **2000**, *25*, 133–139. doi:10.1016/S1464-1895(00)00022-3.

- 568 54. Carmignani, L.; Conti, P.; Disperati, L.; Fantozzi, P.; Giglia, G.; Meccheri, M. Carta Geologica del Parco delle
569 Alpi Apuane. Scala 1:50.000, Massa. *SELCA, Firenze* **2000**.
- 570 55. Molli, G.; Vitale Brovarone, A.; Beyssac, O.; Cinquini, I. RSCM thermometry in the Alpi Apuane (NW Tuscany,
571 Italy): New constraints for the metamorphic and tectonic history of the inner northern Apennines. *Journal of*
572 *Structural Geology* **2018**, *113*, 200–216. doi:10.1016/j.jsg.2018.05.020.
- 573 56. Carmignani, L.; Conti, P.; Cornamusini, G.; Pirro, A. Geological map of Tuscany (Italy). *Journal of Maps* **2013**,
574 *9*, 487–497. doi:10.1080/17445647.2013.820154.
- 575 57. Spalla, M.I.; Zannoni, D.; Marotta, A.M.; Rebay, G.; Roda, M.; Zucali, M.; Gosso, G. The transition from Variscan
576 collision to continental break-up in the Alps: insights from the comparison between natural data and numerical
577 model predictions. *Geological Society, London, Special Publications* **2014**, *405*, 363–400. doi:10.1144/SP405.11.
- 578 58. Manzotti, P.; Zucali, M. The pre-Alpine tectonic history of the Austroalpine continental basement in the
579 Valpelline unit (Western Italian Alps). *Geological Magazine* **2013**, *150*, 153–172. doi:10.1017/s0016756812000441.
- 580 59. Zucali, M.; Manzotti, P.; Diella, V.; Pesenti, C.; Risplendente, A.; Darling, J.; Engi, M. Permian
581 tectonometamorphic evolution of the Dent Blanche Unit (Austroalpine domain, Western Italian Alps).
582 *Rendiconti online Società Geologica Italiana* **2011**, *15*, 133–136.
- 583 60. Roda, M.; Zucali, M.; Li, Z.X.; Spalla, M.I. Pre-Alpine contrasting tectono-metamorphic evolutions within the
584 Southern Steep Belt, Central Alps. *Lithos* **2018**, *310-311*, 31–49. doi:10.1016/j.lithos.2018.03.025.
- 585 61. Camana, G.; Chateigner, D.; Zucali, M.; Artioli, G. The grid-work texture of authigenic microcrystalline quartz
586 in siliceous crust-type (SCT) mineralized horizons. *American Mineralogist* **2002**, *87*, 1128.
- 587 62. Wenk, H.R. Neutron diffraction texture analysis. In *In: Neutron Scattering in Earth Sciences, Reviews in Mineralogy*
588 *and Geochemistry*, 63; Mineralogical Society of America, 2006; pp. 399–426.
- 589 63. Zucali, M.; Tartarotti, P.; Capelli, S.; Ouladdiaf, B. Multiscalar structural study of the ultramafic rocks of the
590 Antrona ophiolite (Pennine Alps). In: (Eds.) Guido Gosso, Maria Iole Spalla, and Michele Zucali, Multiscale
591 structural analysis devoted to the reconstruction of tectonic trajectories in active ma. *Journal of The Virtual*
592 *Explorer* **2012**, *41*, 1–23.
- 593 64. Zucali, M.; Chateigner, D.; Dugnani, M.; Lutterotti, L.; Ouladdiaf, B. Quantitative texture analysis of
594 glaucophanite deformed under eclogite facies conditions (Sesia-Lanzo Zone, Western Alps); comparison
595 between X-ray and neutron diffraction analysis. *Geological Society Special Publications* **2002**, *200*, 239–253.
- 596 65. Siegesmund, S.; Helming, K.; Kruse, R. Complete texture analysis of a deformed amphibolite: comparison
597 between neutron, diffraction and U-stage data. *Journal of Structural Geology* **1994**, *16*, 131–142.
- 598 66. Zucali, M.; Barberini, V.; Voltolini, M.; Ouladdiaf, B.; Chateigner, D.; Mancini, L.; Lutterotti, L. Quantitative 3D
599 microstructural analysis of naturally deformed amphibolite from the Southern Alps (Italy): Microstructures,
600 CPO and seismic anisotropy from a fossil extensional margin. *Special Publication of The Geological Society of*
601 *London* **2015**, *409*, 201–222. doi:10.1144/SP409.5.
- 602 67. Frassi, C.; Musumeci, G.; Zucali, M.; Mazzarini, F.; Rebay, G.; Langone, A. The Cotoncello Shear Zone (Elba
603 Island, Italy): The deep root of a fossil oceanic detachment fault in the Ligurian ophiolites. *Lithos* **2017**,
604 *278-281*, 445–463. doi:10.1016/j.lithos.2017.02.015.
- 605 68. Zucali, M.; Voltolini, M.; Ouladdiaf, B.; Mancini, L.; Chateigner, D. The 3D quantitative lattice and shape
606 preferred orientation of a mylonitised metagranite from Monte Rosa (Western Alps): Combining neutron
607 diffraction texture analysis and synchrotron X-ray microtomography. *Journal of Structural Geology* **2014**, *63*.
608 doi:10.1016/j.jsg.2014.02.011.
- 609 69. Zucali, M.; Fontana, E.; Panseri, M.; Tartarotti, P.; Capelli, S.; Ouladdiaf, B. Submarine lava flow direction
610 revealed by neutron diffraction analysis in mineral lattice orientation. *Geochemistry, Geophysics, Geosystems*
611 **2014**, *15*. doi:10.1002/2013GC005044.
- 612 70. Frischbutter, A.; Neov, D.; Scheffzük, C.; Vrána, M.; Walther, K. Lattice strain measurements on
613 sandstones under load using neutron diffraction. *Journal of Structural Geology* **2000**, *22*, 1587–1600.
614 doi:10.1016/S0191-8141(00)00110-3.

- 615 71. Tartarotti, P.; Zucali, M.; Panseri, M.; Lissandrelli, S.; Capelli, S.; Ouladdiaf, B. Mantle origin of the Antrona
616 serpentinites (Antrona ophiolite, Pennine Alps) as inferred from microstructural, microchemical, and neutron
617 diffraction quantitative texture analysis. *Ofoliti* **2011**, *36*, 167–189.
- 618 72. Lutterotti, L.; Matthies, S.; Wenk, H.R. MAUD (Material Analysis Using Diffraction): a user friendly Java
619 program for Rietveld Texture Analysis and more. Proceedings of the Twelfth International Conference on
620 Textures of Materials (ICOTOM-12); Szpunar J. A., Ed., 1999, Vol. 2, pp. 1599–1605.
- 621 73. Matthies, S.; Wenk, H.R.; Vinel, G.W. Some basic concepts of texture analysis and comparison of three methods
622 to calculate orientation distributions from pole figures. *Journal of Applied Crystallography* **1988**, *21*, 285–304.
623 doi:10.1107/S0021889888000275.
- 624 74. Viani, A.; Gualtieri, A.F.; Puente Orench, I.; Zucali, M. Texture analysis of magnesium potassium phosphate
625 ceramics. *Institut Laue-Langevin (ILL)* **2016**. doi:doi:10.5291/ILL-DATA.1-02-201.
- 626 75. Zucali, M.; Capelli, S.; Chateigner, D.; Ouladiaf, B. Deep mantle related natural microstructures
627 assessed by Quantitative Texture Analysis of natural rocks. *Institut Laue-Langevin (ILL)* **2012**.
628 doi:10.5291/ILL-DATA.5-11-397.
- 629 76. Zucali, M.; Benitez Perez, J.; Chateigner, D.; Gomez-Barreiro, J.; Lutterotti, L.; Ouladdiaf, B. Rheology of the
630 lower crust: Quantitative Texture Analysis of High Pressure - High Temperature rocks from Alps and Iberian
631 Variscan belt. *Institut Laue-Langevin (ILL)* **2014**. doi:10.5291/ILL-DATA.1-02-163.
- 632 77. Babuska, V.; Cara, M. *Seismic anisotropy in the Earth*; Vol. 10, Springer, 1991.
- 633 78. Mainprice, D.; Humbert, M.; Wagner, F. Phase Transformations and Inherited ODFs Implications for
634 Petrophysical Properties. *Textures and Microstructures* **1991**, *14*, 339–345. doi:10.1155/TSM.14-18.339.
- 635 79. Hill, R. The Elastic Behaviour of a Crystalline Aggregate. *Proceedings of the Physical Society. Section A* **1952**,
636 *65*, 349–354. doi:10.1088/0370-1298/65/5/307.
- 637 80. Bachmann, F.; Hielscher, R.; Schaeben, H. Texture analysis with MTEX- Free and open source software toolbox.
638 *Solid State Phenomena*, 2010. doi:10.4028/www.scientific.net/SSP.160.63.
- 639 81. Mainprice, D.; Hielscher, R.; Schaeben, H. Calculating anisotropic physical properties from texture data
640 using the MTEX open-source package. *Geological Society, London, Special Publications* **2011**, *360*, 175–192.
641 doi:10.1144/SP360.10.
- 642 82. Burlini, L.; Marquer, D.; Challandes, N.; Mazzola, S.; Zangarini, N. Seismic properties of highly
643 strained marbles from the Splügenpass, central Alps. *Journal of Structural Geology* **1998**, *20*, 277–292.
644 doi:10.1016/S0191-8141(97)00084-9.
- 645 83. Faccenda, M.; Bressan, G.; Burlini, L. Seismic properties of the upper crust in the central Friuli area (northeastern
646 Italy) based on petrophysical data. *Tectonophysics* **2007**, *445*, 210–226. doi:10.1016/j.tecto.2007.08.004.
- 647 84. Brownlee, S.J.; Hacker, B.R.; Salisbury, M.; Seward, G.; Little, T.A.; Baldwin, S.L.; Abers, G.A. Predicted velocity
648 and density structure of the exhuming Papua New Guinea ultrahigh-pressure terrane. *Journal of Geophysical*
649 *Research: Solid Earth* **2011**, *116*, 1–15. doi:10.1029/2011JB008195.
- 650 85. Connolly, J.A. Multivariable phase diagrams: an algorithm based on generalized thermodynamics. *American*
651 *Journal of Science* **1990**, *290*, 666–718. doi:10.2475/ajs.290.6.666.
- 652 86. pyWerami (v. 0.25) - a stand-alone program to make countour-3D plot from data file generated by the PerpleX
653 program WERAMI or tci file generated by TCInvestigator. <https://github.com/ondrolexa/pywerami/>, 2017.
- 654 87. Zhang, K.J.; Li, Q.H.; Yan, L.L.; Zeng, L.; Lu, L.; Zhang, Y.X.; Hui, J.; Jin, X.; Tang, X.C. Geochemistry
655 of limestones deposited in various plate tectonic settings. *Earth-Science Reviews* **2017**, *167*, 27–46.
656 doi:10.1016/j.earscirev.2017.02.003.
- 657 88. Holland, T.J.B.; Powell, R. An internally consistent thermodynamic data set for phases of petrological interest.
658 *Journal of Metamorphic Geology* **1998**, *16*, 309–344.
- 659 89. Holland, T.J.; Powell, R. An improved and extended internally consistent thermodynamic dataset for phases
660 of petrological interest, involving a new equation of state for solids. *Journal of Metamorphic Geology* **2011**,
661 *29*, 333–383. doi:10.1111/j.1525-1314.2010.00923.x.
- 662 90. Fisher, N.I.; Lewis, T.; Embleton, B.J. *Statistical analysis of spherical data*; Cambridge University Press, 1993; p.
663 329. doi:10.2307/3620138.

- 664 91. Chateigner, D. Reliability criteria in quantitative texture analysis with experimental and simulated orientation
665 distributions. *Journal of Applied Crystallography* **2005**, *38*, 603–611. doi:10.1107/S0021889805013695.
- 666 92. Schaeben, H. Texture analysis of heterogeneous data—a farewell to F-coefficients. *Journal of Structural Geology*
667 **2000**, *22*, 1565–1568.
- 668 93. Wenk, H.R.; Takeshita, T.; Bechler, E.; Erskine, B.G.; Matthies, S. Pure shear and simple shear calcite textures.
669 Comparison of experimental, theoretical and natural data. *Journal of Structural Geology* **1987**, *9*, 731–745.
670 doi:10.1016/0191-8141(87)90156-8.
- 671 94. Burlini, L.C.M.; Rutter, E.H.; Anonymous. Preferred orientation development in hot-pressed synthetic,
672 ultrafine-grained calcite rocks. *Terra Abstracts* **1993**, *5*, Suppl., 288.
- 673 95. Casey, M.; Rutter, E.H.; Schmid, S.M.; Siddans, A.W.B.; Whalley, J.S. Texture development in experimentally
674 deformed calcite rocks. *proc. 5th ICOTOM, Göttstein & Lücke (eds)* **1978**, *2*, 231–240.
- 675 96. Trullenque, G.; Kunze, K.; Heilbronner, R.; Stünitz, H.; Schmid, S.M. Microfabrics of calcite ultramylonites as
676 records of coaxial and non-coaxial deformation kinematics: Examples from the Rocher de l'Yret shear zone
677 (Western Alps). *Tectonophysics* **2006**, *424*, 69–97. doi:10.1016/j.tecto.2006.06.004.
- 678 97. Schmid, S.M.; Casey, M.; Starkey, J. The microfabric of calcite tectonites from the Helvetic Nappes (Swiss Alps).
679 *in: Thrust and Nappe Tectonic, Geological Society of London* **1981**, pp. 151–158.
- 680 98. Ratschbacher, L.; Wenk, H.R.; Sintubin, M. Calcite textures; examples from nappes with strain-path partitioning.
681 *Journal of Structural Geology* **1991**, *13*, 369–384.
- 682 99. Erskine, B.G.; Heidelbach, F.; Wenk, H.R. Lattice preferred orientations and microstructures of deformed
683 Cordilleran marbles: correlation of shear indicators and determination of strain path. *Journal of Structural*
684 *Geology* **1993**, *15*, 1189–1205. doi:10.1016/0191-8141(93)90163-5.
- 685 100. Leiss, B.; Siegesmund, S.; Weber, K. Texture Asymmetries as Shear Sense Indicators in Naturally Deformed
686 Mono- and Polyphase Carbonate Rocks. *Textures and Microstructures* **1999**, *33*, 61–74. doi:10.1155/tsm.33.61.
- 687 101. Pieri, M.; Burlini, L.; Kunze, K.; Stretton, I.; Olgaard, D.L. Rheological and microstructural evolution of Carrara
688 marble with high shear strain: Results from high temperature torsion experiments. *Journal of Structural Geology*
689 **2001**, *23*, 1393–1413.
- 690 102. De Wall, H.; Bestmann, M.; Ullemeyer, K. Anisotropy of diamagnetic susceptibility in Thassos
691 marble: A comparison between measured and modeled data. *In Journal of Structural Geology; Leiss,*
692 *B.; Ullemeyer, K.; Weber, K., Eds.; Pergamon. Oxford, International., 2000; Vol. 22, pp. 1761–1771.*
693 doi:10.1016/S0191-8141(00)00105-X.
- 694 103. Ebert, A.; Herwegh, M.; Pfiffner, A. Cooling induced strain localization in carbonate mylonites within
695 a large-scale shear zone (Glarus thrust, Switzerland). *Journal of Structural Geology* **2007**, *29*, 1164–1184.
696 doi:10.1016/j.jsg.2007.03.007.
- 697 104. Demurtas, M.; Smith, S.A.; Prior, D.J.; Spagnuolo, E.; Di Toro, G. Development of crystallographic preferred
698 orientation during cataclasis in low-temperature carbonate fault gouge. *Journal of Structural Geology* **2019**,
699 *126*, 37–50. doi:10.1016/j.jsg.2019.04.015.
- 700 105. Fernández, F.J.; Brown, D.; Álvarez-Marrón, J.; Prior, D.J.; Pérez-Estaún, A. Microstructure and lattice preferred
701 orientation of calcite mylonites at the base of the southern Urals accretionary prism. *Journal of the Geological*
702 *Society* **2004**, *161*, 67–79. doi:10.1144/0016-764903-027.
- 703 106. Parsons, A.J.; Law, R.D.; Lloyd, G.E.; Phillips, R.J.; Searle, M.P. Thermo-kinematic evolution of the
704 Annapurna-Dhaulagiri Himalaya, central Nepal: The Composite Orogenic System. *Geochemistry, Geophysics,*
705 *Geosystems* **2016**, *17*, 1511–1539. doi:10.1002/2015GC006184.
- 706 107. Wells, R.K.; Holyoke, C.W.; Newman, J.; Kronenberg, A. Lattice-preferred orientation development in
707 experimental and natural fine-grained dolomite shear zones. *Journal of Structural Geology* **2019**, *128*, 103874.
708 doi:10.1016/j.jsg.2019.103874.
- 709 108. Leiss, B.; Weiss, T. Fabric anisotropy and its influence on physical weathering of different types of Carrara
710 marbles. *Journal of Structural Geology*, 2000, Vol. 22, pp. 1737–1745. doi:10.1016/S0191-8141(00)00080-8.

- 711 109. Barnhoorn, A.; Bystricky, M.; Burlini, L.; Kunze, K. The role of recrystallisation on the deformation behaviour of
712 calcite rocks: Large strain torsion experiments on Carrara marble. *Journal of Structural Geology* **2004**, *26*, 885–903.
713 doi:10.1016/j.jsg.2003.11.024.
- 714 110. Oesterling, N.; Heilbronner, R.; Stünitz, H.; Barnhoorn, A.; Molli, G. Strain dependent variation of
715 microstructure and texture in naturally deformed Carrara marble. *Journal of Structural Geology* **2007**, *29*, 681–696.
716 doi:10.1016/j.jsg.2006.10.007.
- 717 111. Negrini, M.; Smith, S.A.; Scott, J.M.; Tarling, M.S. Microstructural and rheological evolution of calcite mylonites
718 during shear zone thinning: Constraints from the Mount Irene shear zone, Fiordland, New Zealand. *Journal of*
719 *Structural Geology* **2018**, *106*, 86–102. doi:10.1016/j.jsg.2017.11.013.
- 720 112. De Bresser, J.H. Calcite c-axis textures along the Gavarnie thrust zone, central Pyrenees. *Geologie en Mijnbouw*
721 **1989**, *68*, 367–375.
- 722 113. Anselmetti, F.S.; Eberli, G.P. Sonic Velocity in Carbonate Sediments and Rocks. *Carbonate Seismology* **1997**, pp.
723 53–74. doi:10.1190/1.9781560802099.ch4.
- 724 114. Bassinot, F.C.; Marsters, J.C.; Mayer, L.A.; Wilkens, R.H. Velocity anisotropy in calcareous sediments
725 from Leg 130, Ontong Java Plateau. *Proc., scientific results, ODP, Leg 130, Ontong Java Plateau* **1993**.
726 doi:10.2973/odp.proc.sr.130.041.1993.
- 727 115. Park, S.; Ishii, M. Near-surface compressional and shear wave speeds constrained by body-wave polarization
728 analysis. *Geophysical Journal International* **2018**. doi:10.1093/gji/ggy072.
- 729 116. Cloos, M. Lithospheric buoyancy and collisional orogenesis: subduction of oceanic plateaus, continental
730 margins, island arcs, spreading ridges, and seamounts. *Geological Society of America Bulletin* **1993**, *105*, 715–737.
731 doi:10.1130/0016-7606(1993)105<0715:LBACOS>2.3.CO.
- 732 117. Rudnick, R.L.; Fountain, D.M. Nature and composition of the continental crust: A lower crustal perspective.
733 *Reviews of Geophysics* **1995**, *33*, 267–309. doi:10.1029/95RG01302.